Energy, Volume 330, September 2025, Article number 136879
DOI:10.1016/j.energy.2025.136879

Optimization of dual-module floating photovoltaic arrays: Layout configuration and damping mechanisms for enhanced stability and energy performance

Zhi Zheng[a, b], Jianjian Hu[b], Qiang Huang[c], Peng Jin[b], Yifeng Yang[d], Luofeng Huang[e], Zhaomin Zhou[f], Binzhen Zhou[a, b, *]

[a] *State Key Laboratory of Subtropical Building and Urban Science, South China University of Technology, Guangzhou 510641, China*

[b] *School of Civil Engineering and Transportation, South China University of Technology, Guangzhou 510641, China*

[c] *School of Marine Science and Engineering, South China University of Technology, Guangzhou, 511442, China*

[d] *Department of Mechanical Engineering, University College London, London, WC1E 7JE, United Kingdom*

[e] *Faculty of Engineering and Applied Sciences, Cranfield University, Cranfield MK43 0AL, United Kingdom*

[f] *PowerChina Renewable Energy Co., LTD., Beijing, 100101, China*

Abstract

Floating Photovoltaic (FPV) systems are a promising solution for offshore renewable energy, with modular FPV arrays offering significant potential for large-scale deployment. However, the development of FPV systems is hindered by insufficient understanding of their hydrodynamic performance, which affects stability and energy efficiency. This study proposes a dual-module FPV array combining box-type and semi-submersible modules to improve hydrodynamic stability under mild wave conditions in the South China Sea. The effects of array layout and PTO damping are examined under various wave conditions. The system is optimized to balance energy harvesting and motion control, and its performance is further evaluated under irregular waves at selected operational sites. Results indicate that the dual-module design effectively leverages the hydrodynamic characteristics of both module types, reducing motion responses and dynamic loads. The incorporation of optimal PTO damping further enhances system stability and energy efficiency by effectively suppressing pitch and heave motions, with maximum reductions of 31.43% and 41.56%, respectively, under the selected operational wave conditions. While damping remains effective under head-on waves, its performance slightly decreases under oblique waves, underscoring the importance of aligning the array with the predominant wave direction. Additionally, integrating a wave energy PTO system into the FPV array enables wave power to supplement solar energy, contributing 17.04% of the total energy output at the selected operational sites. The proposed FPV system offers a practical solution for stabilizing floater motion, enhancing solar power generation, and capturing wave energy, advancing the feasibility of FPV technology for large-scale offshore applications.

* Corresponding author
E-mail address: zhoubinzhen@scut.edu.cn (B. Zhou)

Keyword: Marine Renewable Energy; Floating Photovoltaic; Wave Energy Converters; Dual-modules; Hybrid System; Array Configuration

1. Introduction

Photovoltaic (PV) technology is one of the most promising renewable energy systems due to its ease of deployment, cost efficiency, and adaptability across various applications. It is projected to become the most widely adopted renewable energy technology [1]. However, the rapid expansion of land-based PV systems, which require approximately 165 acres per GW [2], has resulted in increased pressure on land resources, often conflicting with other uses such as agriculture, infrastructure, and transportation. To address these land use constraints, Floating Photovoltaic (FPV) systems have emerged as a promising alternative. Compared to lakes and reservoirs with limited space, coastal and offshore seas offer considerably more area, enabling large-scale FPV deployment [3][4]. Modular FPV designs, which have proven effective in inland waters, employ interconnected floaters to form scalable energy systems, a concept that is now being extended offshore [5]. Sea trials by various manufacturers, such as the Dutch company SolarDuck, the Chinese company CIMC Raffles, and COEC Co., Ltd., have validated the feasibility of offshore modular FPV systems [6]. However, offshore environments impose complex dynamic loads, with wave loads predominantly affecting system stability and motion responses [7], further impacting system performance and operational stability [8].

Consequently, current research has increasingly focused on the hydrodynamics of array layouts and multi-body interactions, which are crucial for advancing the performance of FPV systems. Li et al. [9] studied a multi-body FPV with four hexagonal modules and found that hydrodynamic coupling significantly influences floater motion and overall system behavior, highlighting the importance of module arrangements. Xu et al. [10] investigated the hydrodynamic performance of three FPV array arrangements and found that the rectangular array exhibited the greatest stability and was least affected by variations in load incident angles. Within FPV arrays, research has also expanded to explore the impact of floater geometries on system dynamics. A variety of floater geometries, such as semi-submersible structures [11][12], box-pontoon structures [13], lattice-structured platforms [14][15] and novel floating modules [16][17], have been proposed and investigated. The connection methods between floating bodies, which have been extensively studied, are mainly classified into three categories: rigid [18][19], flexible [20], and hinged connections [21]. Rigid connections enhance structural stability but may induce high internal stresses [22]. Flexible connections improve compliance and wave adaptability but require precise design [23]. Hinged connections, which allow controlled articulation, have drawn particular attention for their balance of adaptability and structural integrity [24]. The relative motion between adjacent modules in hinged FPV systems

exhibits similarities to flap-type wave energy converters [25][26], suggesting the potential for integrating PTO systems within the connectors to enable wave energy absorption while enhancing motion control by increasing the elastic stiffness and damping of the connections [27]. While studies on multi-body raft-type WECs have primarily emphasized energy absorption efficiency, FPV array design requires greater emphasis on motion response control and the integration of wave energy capture, an area that remains underexplored.

In previous studies [28], a large single-row FPV structure interconnected by an articulated PTO system was proposed, with its motion characteristics and power performance evaluated. Results show that suitable damping or stiffness coefficients effectively function as motion attenuators, reducing motion response, especially in multi-float cases. The proposed FPV array also demonstrates great potential for the synergistic utilization of solar and wave energy. However, prior research focused solely on a single-row configuration and did not explore its extension to multiple array configurations or varying wave directions. Moreover, while the incorporation of the PTO system effectively reduces floater motion, the pitch response remains relatively large, particularly for floaters at the front of the array, adversely affecting system stability and photovoltaic energy capture. According to technical reviews [29], rigid-pontoon offshore FPV systems typically experience a 7.22% reduction in annual solar energy output due to dynamic motion, with maximum losses observed up to 15% under more severe conditions. Therefore, further strategies should be explored to mitigate floater motion, particularly rotational responses, to enhance solar irradiance on the panels. One potential approach is deploying a floating breakwater to create a sheltered zone, offering protection for the FPV array. Yang et al. [30] conducted wave tank experiments to assess the hydrodynamic performance of two FPV floaters, with a breakwater placed in front of the FPV array to mitigate direct wave interaction with solar units. Results showed that the breakwater reduced wave height by over 50%, protecting the system and enhancing stability and energy efficiency. Tay et al. [31] proposed a hybrid system combining a floating breakwater with wave energy converters and analyzed four configurations around offshore FPV systems. Results show that the FB-WEC-BOX configuration, which surrounds the FPV array like a box, was the most effective in mitigating hydro-elastic responses, though all configurations showed reduced effectiveness in long waves, particularly at a wave period of 5 s. Both studies explored the deployment of additional marine structures in the wave-exposed direction of the FPV array to dissipate wave energy and shield the solar units from excessive hydrodynamic forces. Liu et al. [32] proposed a hybrid modular floating structure system consisting of inner semi-sub modules and outermost box-type modules. The inner modules are linked by hinges with linear pitch springs, while the outer modules function as floating breakwaters with PTO damping to absorb wave energy

through relative pitch motion. Utilizing the distinct hydrodynamic properties of different floaters, this design enhances stability and energy capture, with potential for application in FPV arrays. However, research on the practical implementation and optimization of this design in FPV arrays remains limited.

To address this gap, this study proposes a dual-module FPV array integrating semi-submersible and box-type modules to improve hydrodynamic stability and energy efficiency. The semi-submersible modules improve overall stability, while the box-type modules attenuate incoming waves, with PTO damping further reducing motion and simultaneously capturing wave energy. To investigate the expansibility of the proposed FPV array, both longitudinal and lateral extensions are examined, considering their impact on hydrodynamic performance. Additionally, an optimal PTO strategy is developed to minimize motion responses and enhance wave energy utilization under varying wave conditions. Its novelties lie in the systematic investigation of the innovative dual-module configuration of FPV arrays, examining their expansibility, and the development of an integrated PTO strategy that enhances both motion control and wave energy capture. The optimized array is further evaluated under irregular wave conditions at two selected sites, demonstrating its potential for offshore deployment. These findings offer valuable insights into novel floating photovoltaic designs, highlighting their deployment and scalability in marine environments and their role in advancing solar-wave energy integration.

The structure of the paper is organized as follows: Section 2 provides an overview of the methodology, which is validated through model testing in Section 3. Section 4 details the configuration of the dual-module FPV array model and the selection criteria for its design. In Section 5, the impact of array layout and PTO damping on the connectors is examined under various wave directions and regular wave conditions. The dynamic behavior and power generation performance of the optimized FPV array are further evaluated under irregular wave conditions at two selected operational sites. Finally, Section 6 presents the main conclusions.

2. Description of proposed dual-module FPV array model

The schematic diagram of the novel floating photovoltaic array consists of two types of floating modules: box-type and semi-submersible type, illustrated in Figure 1. These floating bodies are aligned along the north–south direction, with photovoltaic panels mounted on top and tilted southward at a fixed installation angle β_0. The individual motion response RAOs for the two module types are shown in Figure 2 to highlight their distinct hydrodynamic characteristics. The proposed FPV array is designed for the mild marine environment of the South China Sea, where the mean wave period typically ranges from 5-10 s [33]. Two potential operation locations are selected in this study: Location A (114°58′E, 21°16′N), Location B

(110°39′E, 19°20′N), with the average wave periods of them are 5.30 s and 6.45 s, respectively, according to the hindcast data provided by National Ocean Technology Center (NOTC).Within this wave period range, as shown in Figure 2, the semi-submersible module demonstrates superior hydrodynamic performance, exhibiting lower pitch and heave motion compared to the box-type floater due to its smaller waterline area. In contrast, the box-type module, with its larger water-retaining area and resonant period aligning with the wave frequency range, proves more effective in dissipating wave energy. Based on these findings, the box-type modules are strategically positioned at the front and rear of the array to attenuate incoming waves and provide shielding effects, thereby significantly reducing the motion responses of the central modules. Meanwhile, the semi-submersible modules, owing to their superior hydrodynamic stability, are arranged in the center to enhance overall system performance. This dual-module FPV array layout is therefore initially proposed, as depicted in Figure 1. In terms of this arrangement, the box-shaped modules, located on both sides of the array, are connected to the inner modules by hinges with the linear pitch power take-off (PTO) system, allowing them to serve as both attenuators and wave energy converters. Due to shielding effects, the motion responses of the inner modules are usually less pronounced than those of the outermost modules. Therefore, the connectors between the semi-submersible type inner modules are equipped with the ideal frictionless ball joints, which allow for three rotational degrees of freedom, providing some flexibility and reducing stress on the connections. The catenary mooring lines are arranged on the box-type modules at the front and rear of the array to restore the system to its original position. The mooring arrangement was considered based on the equivalent mooring stiffness matrix, which was calculated using an open-source mooring analysis program [34].

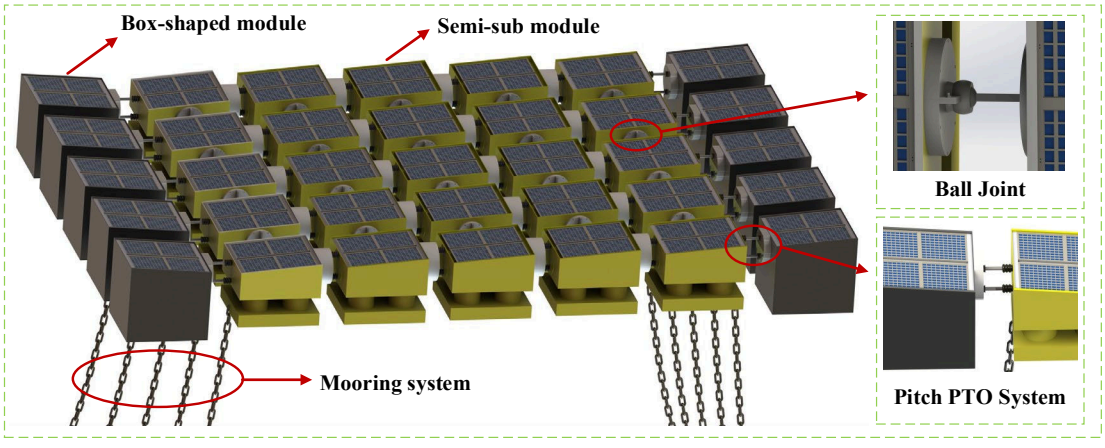

Figure 1 Design diagram of the novel floating photovoltaic array system

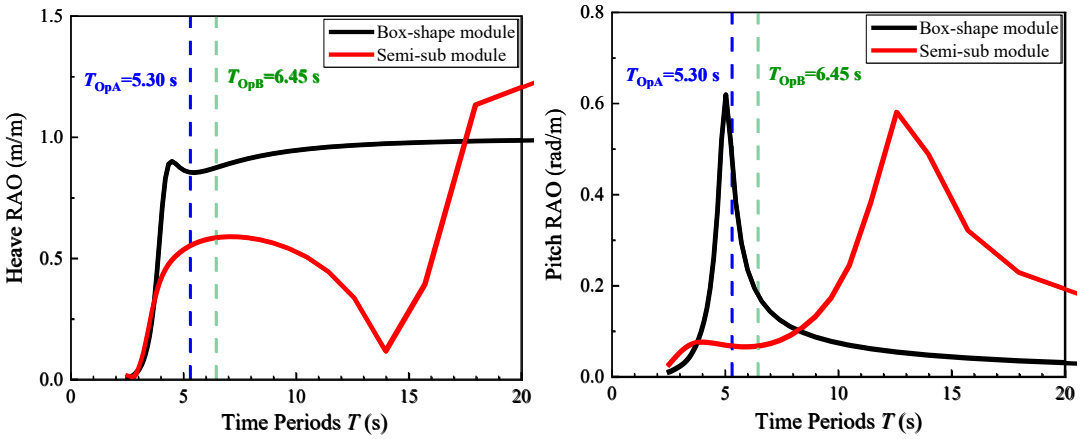

(a) Heave RAO (b) Pitch RAO

Figure 2 Motion response RAOs between Box-type and Semi-submersible floating modules

The design layout of the dual-module FPV array system is shown in Figure 3, with its geometric properties presented in Table 1. The geometric parameters of the box-type floater were determined based on previous studies [28] on wave interactions with box-type floaters. The dimensions of the semi-submersible floater were scaled from Liu et al. [35] to ensure compatibility with the proposed array system. This study accounts for the interaction between multiple floating bodies and multi-directional waves, considering roll, pitch, and yaw motions of the array. Thus, the array cannot be simplified to a single-row FPV array. Connecting adjacent box-type modules with ball joints enables the array to better handle oblique wave incidence conditions. The hydrodynamic and energy performance of the proposed FPV array under various wave conditions, along with its lateral and longitudinal expansibility, will be discussed in the following sections.

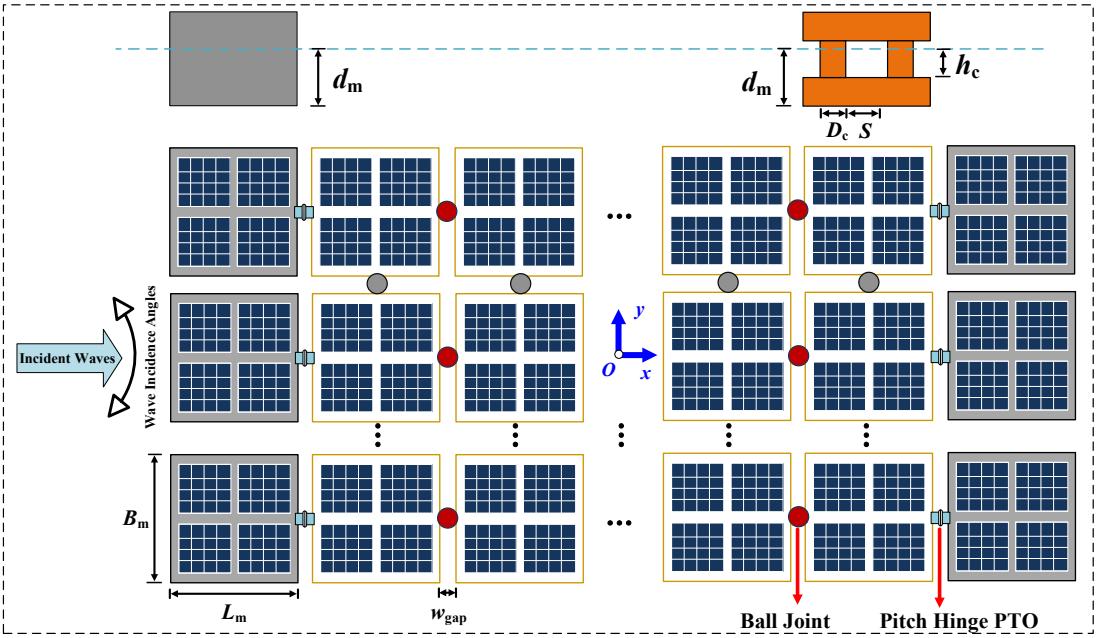

Figure 3 Sketch and configuration of the dual-module FPV array system

Table 1 Key parameters of the FPV array system

Item	Value and unit
Floater Draft d_m (For both modules)	4 m
Floater Length L_m (For both modules)	10 m
Floater Width B_m (For both modules)	10 m
Diameter of columns D_c (For semi-sub type module)	3 m
Spacing between columns S (For semi-sub type module)	2 m
Submerged Column Height h_c	2 m
Gap Width w_{gap}	1 m
Mass of the semi-sub type module M_s	2.25E+05 kg
Mass of the box-type module M_b	4.00E+05 kg
Pitch moment of inertia $I_{s\text{-}yy}$ (For semi-sub type module)	2.00E+05 kg·m^2
Roll moment of inertia $I_{s\text{-}xx}$ (For semi-sub type module)	2.00E+05 kg·m^2
Yaw moment of inertia $I_{s\text{-}zz}$ (For semi-sub type module)	2.01E+06 kg·m^2
Pitch moment of inertia $I_{b\text{-}yy}$ (For box-type module)	2.57E+05 kg·m^2
Roll moment of inertia $I_{b\text{-}xx}$ (For box-sub type module)	2.57E+05 kg·m^2
Yaw moment of inertia $I_{b\text{-}zz}$ (For box-sub type module)	3.08E+06 kg·m^2
Pitch/roll viscous damping $b_{s\text{-}vis4}$/$b_{s\text{-}vis5}$ (For semi-sub type module)	3.20E+05 N·m·s/rad
Heave viscous damping $b_{s\text{-}vis3}$ (For semi-sub type module)	1.38E+05 N·s/m
Pitch/roll viscous damping $b_{b\text{-}vis4}$/$b_{b\text{-}vis5}$ (For box-sub type module)	6.56E+05 N·m·s/rad
Heave viscous damping $b_{b\text{-}vis3}$ (For box-sub type module)	1.07E+05 N·s/m

In this study, the Hi-MOH LR7-72HGD-575M photovoltaic modules, manufactured by LONGi, a globally recognized producer, are applied. This model is designed for offshore applications, featuring corrosion-resistant materials and enhanced durability. A schematic of the selected PV module is presented in Figure 4, with key parameters summarized in Table 2. Based on the module dimensions, 32 units are arranged on the floating platform in an 8 × 4 layout, resulting in a spatial utilization rate of approximately 86.4%. The listed electrical performance parameters in Table 2 are specified under either Standard Test Conditions (STC) or Nominal Operating Cell Temperature (NOCT) conditions. STC refers to a solar irradiance of 1000 W/m², a cell temperature of 25 °C, and an air mass of 1.5, while NOCT corresponds to an ambient temperature of 20 °C, an irradiance of 800 W/m², and a wind speed of 1 m/s.

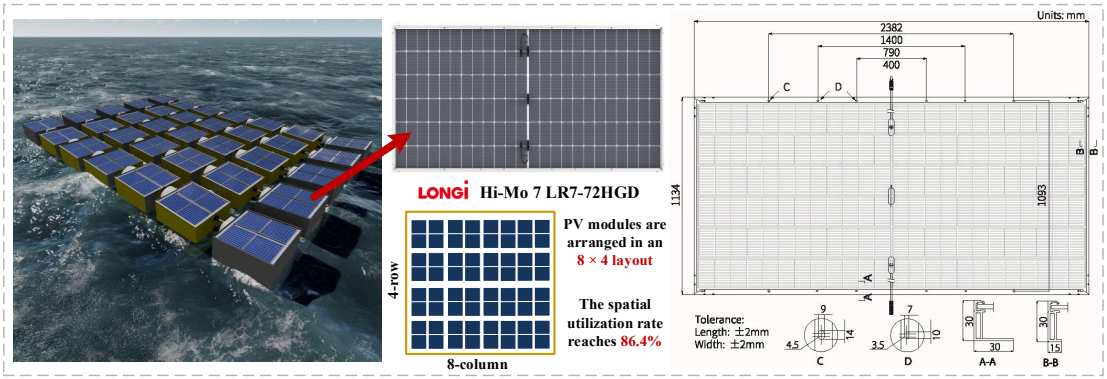

Figure 4 Schematic diagram and main dimensions of the photovoltaic module

Table 2 Key parameters of the photovoltaic module [36]

Parameter	Value
Main dimensions (mm)	2382×1134×30
Mass (kg)	33.5
Maximum photoelectric conversion efficiency η	22.6%
Maximum power under STC/NOCT (W)	575/437.7
Open-circuit voltage under STC/NOCT (V)	51.3/48.75
Short circuit current under STC/NOCT (A)	14.14/11.35
Voltage at maximum power under STC/NOCT (V)	43.11/40.97
Current at maximum power under STC/NOCT (A)	13.34/10.68
Operational temperature (°C)	-40 ~ +80
Nominal operating cell temperature (°C)	45±2

3. Numerical model

3.1 Hydrodynamics

The interaction of multiple floating bodies with incident waves generates diffracted and radiated waves, resulting in complex mutual interference in wave propagation. In this study, potential flow theory is used to model the fluid motion around the bodies, assuming the surrounding fluid is incompressible, inviscid, and irrotational. The velocity potential, satisfying the Laplace equation, is linearized and divided into three main components: incident velocity potential ϕ_I, total radiation velocity potential ϕ_R, and diffraction velocity potential ϕ_D, which can be written as follows:

$$\phi(x,t) = \mathrm{Re}[\eta_0\varphi_0(x)e^{-i\omega_0 t}] + \mathrm{Re}\sum_{k=1}^{6}\sum_{m=1}^{n}(\eta_j^m\varphi_j^m(x)e^{-i\omega_0 t}) + \mathrm{Re}[\eta_7\varphi_7(x)e^{-i\omega_0 t}] \quad (1)$$

where ω_0 is the angular frequency of the incident wave, and η_0=η_7 represents the wave amplitude. φ_0 and φ_7 denote the unit incident potential and the unit diffraction wave potential, respectively. n represents the total number of the floating body. φ_k^m (k=1,2…6, m=1, 2, …, n)

is the unit radiation wave potential corresponding to the six degrees of freedom of each floating body while η_k^m (k=1,2…6, m=1, 2, …, n) represents the associated motion amplitude.

The governing equation for the velocity potential, along with the corresponding linearized boundary conditions on the free surface S_f (z=0), the wetted body surface S_b, and the seabed S_d (z=−h), is expressed as follows:

$$\nabla^2\phi = 0 \tag{2}$$

$$\left.\begin{aligned} \frac{\partial\phi}{\partial z} - \frac{\omega^2}{g}\phi = 0 \quad & z = 0 \\ \frac{\partial\phi}{\partial n} = V \quad & \text{on } S_b \\ \frac{\partial\phi}{\partial z} = 0 \quad & \text{on } S_d \end{aligned}\right\} \tag{3}$$

In this study, the higher-order boundary element method code WAFDUT, developed by Teng et al. [37], is used to solve the velocity potential, which accounts for the coupled hydrodynamic effects of the multi-float system.

3.2 Constrained motion equations

With the total velocity potential ϕ obtained, the pressure distribution on the wetted surface of the floating body is calculated using the linearized Bernoulli equation, as shown below:

$$\boldsymbol{f} = -\rho\iint_{S_b}\left[gz - \mathrm{i}\omega(\phi_i + \phi_d + \phi_r)\right] - \rho g\iint_{S_b}\left[\boldsymbol{\xi} + \boldsymbol{\alpha}\cdot(\boldsymbol{x} - \boldsymbol{x}_0)\right]\cdot\boldsymbol{n}_3\boldsymbol{n}\mathrm{d}s \tag{4}$$

where ρ represents the fluid density, and the second term describes the restoring force caused by the displacement of the floating bodies from their equilibrium position.

The wave excitation force can be obtained by integrating both the incident and diffraction pressures on the wetted body surface, along with the hydrodynamic forces generated by the oscillatory motion. The added mass and radiation damping coefficients are derived by integrating the dynamic pressures induced by the oscillatory motion of the bodies on the wetted surface [38]. With these hydrodynamic coefficients, the constrained motion equation of the multi-floating-body system in the frequency domain can be expressed as:

$$\begin{bmatrix} -\omega^2(\mathbf{M}+\mathbf{a}) + \mathrm{i}\omega(\mathbf{b}+\mathbf{b}_{PTO}+\mathbf{b}_{vis}) + \mathbf{k}_r + \mathbf{k}_m & \mathbf{C}_X^T \\ -\omega^2\mathbf{C}_X & \mathbf{0} \end{bmatrix}\begin{bmatrix} \boldsymbol{\xi} \\ \boldsymbol{f}_L \end{bmatrix} = \begin{bmatrix} \mathbf{F}_{ex} \\ \mathbf{0} \end{bmatrix} \tag{5}$$

where $\mathbf{a}$=a_{ij} and $\mathbf{b}$=b_{ij} (i, j=1, 2…6n) represent the 6n×6n added mass matrix and radiation damping matrix, respectively. $\mathbf{b}_{vis}$ is the viscous damping matrix and $\mathbf{b}_{PTO}$ is the hinge connector damping coefficient. $\mathbf{k}_r$ and $\mathbf{k}_m$ are the hydrostatic restoration and equivalent mooring stiffness matrices, respectively. $\boldsymbol{\xi}$ is the 1×6n vector of the system's motion response. $\boldsymbol{f}_L$ is the 5Q×1

matrix, which represents the forces and moments caused by the constraints between buoys, where Q denotes the number of hinge joint connectors. $\mathbf{F}_{ex}$ is the $6n\times1$ vector of the wave excitation force acting on the system. The constraint matrix $\boldsymbol{C}_x$ of the system is the $5Q\times6n$ matrix, and more details of the constraints matrix can be found in Ref [39].

The time-domain constrained dynamic equation for the multi-floating-body system can be described using the Cummins formulation [40]:

$$\begin{bmatrix} \boldsymbol{M}+\mathbf{a}(\infty) & \boldsymbol{C}_{\mathrm{X}}{}^{T} \\ \boldsymbol{C}_{\mathrm{X}} & 0 \end{bmatrix}\begin{bmatrix} \ddot{\boldsymbol{\xi}}(t) \\ \boldsymbol{f}_{\mathrm{L}} \end{bmatrix}=\begin{bmatrix} -\int_{-\infty}^{t}\boldsymbol{\kappa}(t-\tau)\dot{\mathbf{X}}(t)d\tau-\mathbf{k}_{\mathrm{r}}\mathbf{X}(t)+\boldsymbol{F}^{\mathrm{Wave}}(t)+\boldsymbol{F}^{\mathrm{Moor}}(t)+\boldsymbol{F}^{\mathrm{vis}}(t)+\boldsymbol{F}^{\mathrm{PTO}}(t) \\ 0 \end{bmatrix} \quad (6)$$

where $\mathbf{a}(\infty)$ is the added mass matrix at infinite wave frequency, $\boldsymbol{\kappa}(t-\tau)$ is the matrix of the radiation impulse response function [41].

3.3 Energy capture estimation under wave-interaction

The solar irradiance incident on the tilted surface is calculated based on the direct, diffuse, and reflected irradiance components measured on the horizontal plane [42]:

$$G_{\beta}=B_{\mathrm{h}}R_{\mathrm{b}}+D_{\mathrm{h}}R_{\mathrm{d}}+G_{\mathrm{h}}\rho_{w}R_{\mathrm{r}} \quad (7)$$

where B_{h}, D_{h} and G_{h} represent the direct beam, diffuse, and reflected solar radiation components irradiances on the horizontal plane, respectively. R_{b} denotes the ratio of beam irradiance on the tilted surface to that on the horizontal plane, while R_{d} represents the corresponding ratio for diffuse irradiance. The term $R_{\mathrm{r}}\rho_{\mathrm{w}}$ accounts for sea-surface reflected radiation incident on the tilted surface, with ρ_{w} being the reflection coefficient of the water surface. The basic parameters of solar irradiance components used in this study are provided in Table 3.

R_{b} can be calculated using the following equation:

$$R_{\mathrm{b}}=\frac{B_{\mathrm{n}}\cos\theta_{\beta}}{B_{\mathrm{n}}\cos\theta} \quad (8)$$

where B_{n} is the normal incident beam irradiance, while θ and θ_{b} are the incidence angles of solar radiation on the horizontal and tilted planes, respectively, and can be obtained as:

$$\begin{aligned}\cos\theta_{\beta}=&\cos(\beta)(\sin\delta\sin\varphi+\cos\delta\cos\varphi\cos\omega)+\\&\sin(\beta)(\cos\delta\sin\gamma\sin\omega+\cos\delta\sin\varphi\cos\gamma\cos\omega-\sin\delta\cos\varphi\cos\gamma)\end{aligned} \quad (9)$$

where β is the tilt angle, δ is the declination of the sun, φ is the geographic latitude, γ is the surface azimuth angle and ω is the hour angle. In the special case of β=0, Eq. (9) reduces to the expression $\cos\theta$.

The diffuse radiation is modeled using an isotropic model, assuming uniform sky distribution:

$$R_{d}=\frac{1+\cos\beta}{2} \quad (10)$$

The reflected radiation is considered to be isotropic and the R_{r} can be calculated as:

$$R_{\mathrm{r}}=\frac{1-\cos\beta}{2} \tag{11}$$

The power output of the FPV fluctuates with wave-induced motions, with rotation being the key factor affecting the solar irradiance on the PV modules. In cases with multi-directional incident waves, the pitch, roll, and yaw motions of each float collectively influence the system's dynamic response, with pitch and roll primarily affecting tilt and stability, while yaw impacts directional alignment [43]. The instantaneous tilt angle β_{FPV} and azimuth angle γ_{FPV} of each FPV module are determined by the platform's spatial orientation under wave-induced motion, and can be expressed as:

$$\beta_{\mathrm{FPV}}(t)=\frac{\left|\vec{n}_{\mathrm{horizontal}}\right|}{\vec{n}_{z}}=\arctan\left(\frac{\sqrt{\sin^{2}(\theta_{\mathrm{pitch}}(t)-\beta_{0})+(\sin\theta_{\mathrm{roll}}(t)\cdot\cos(\theta_{\mathrm{pitch}}(t)-\beta_{0}))^{2}}}{\cos\theta_{\mathrm{roll}}(t)\cdot\cos(\theta_{\mathrm{pitch}}(t)-\beta_{0})}\right) \tag{12}$$

$$\begin{aligned}\gamma_{\mathrm{FPV}}(t)=\arctan 2[&\sin\theta_{\mathrm{yaw}}(t)\cdot\sin(\theta_{\mathrm{pitch}}(t)-\beta_{0})-\cos\theta_{\mathrm{yaw}}(t)\cdot\cos(\theta_{\mathrm{pitch}}(t)-\beta_{0})\cdot\sin\theta_{\mathrm{roll}}(t),\\&-\cos\theta_{\mathrm{yaw}}(t)\cdot\sin(\theta_{\mathrm{pitch}}(t)-\beta_{0})-\sin\theta_{\mathrm{yaw}}(t)\cdot\cos(\theta_{\mathrm{pitch}}(t)-\beta_{0})\cdot\sin\theta_{\mathrm{roll}}(t)]\end{aligned} \tag{13}$$

whereβ_0 denotes the initial tilt angle of the photovoltaic panels relative to the horizontal plane. θ_{roll}, θ_{pitch} and θ_{yaw} represent the wave-induced roll, pitch, and yaw motions of the platform, respectively.

By substituting Eq. (12) and Eq. (13) into Eq. (1), the solar irradiance on the FPV of an individual floating body can be reformulated as:

$$G_{\beta_{\mathrm{FPV}}}(t)=B_{\mathrm{h}}\frac{\cos\theta_{\beta_{\mathrm{FPV}}}[\beta_{\mathrm{FPV}}(t),\ \gamma_{\mathrm{FPV}}(t)]}{\cos\theta}+D_{\mathrm{h}}\frac{1+\cos\beta_{\mathrm{FPV}}(t)}{2}+G_{\mathrm{h}}\rho_{w}\frac{1-\cos\beta_{\mathrm{FPV}}(t)}{2} \tag{14}$$

Based on the calculated solar irradiance on the PV module, the power output can be estimated as follows [44]:

$$P_{\mathrm{PV}}(t)=\eta A_{\mathrm{PV}}G_{\beta_{\mathrm{FPV}}}[1-0.005(T_{\mathrm{c}}-25)] \tag{15}$$

where η is the photoelectric conversion efficiency of PV module, A_{PV} is the total array area, and T_{C} is the panels' operation temperature. The PV module temperature is assumed constant at the nominal operating cell temperature of about 45 °C.

Raft-type wave energy converters like the "Pelamis" often use hydraulic PTO systems for their reliability and ability to withstand large forces. Linear PTO models have been shown to capture 80–90% of the energy efficiency of full hydraulic systems [45], making them a practical solution for preliminary design and hydrodynamic evaluation. In this study, the damping coefficients of the articulated system are assumed to be linear PTO damping b_{PTO}, which attenuates the response without affecting the structure's resonance frequency. Wave energy captured from the relative rotational motion between two adjacent floating bodies can be obtained as follows [46]:

$$P_{\text{wave}}(t) = \tau_{\text{PTO}} \Delta\dot{\theta}_{\text{pitch}}(t) = b_{\text{PTO}} \Delta\dot{\theta}_{\text{pitch}}{}^{2}(t) \tag{16}$$

where τ_{PTO} represents the reaction torque of the PTO system at the hinge.

To enable rapid optimization, frequency-domain analysis offers an efficient approach [47]. Referring to the motion-induced power loss level (PL) empirical equation proposed by Huang et al. [48], the photovoltaic energy output PW_{solar} can be preliminary estimated using the following equation, considering both roll and pitch motion amplitudes of the i-th floater in frequency-domain, assuming vertical solar incidence and constant module efficiency without temperature effects:

$$PW_{\text{solar}} = \eta A_{\text{PV}} (B_{\text{h}} + D_{\text{h}} + G_{\text{h}})(1 - \sqrt{1 - (\cos\theta_{i\,\text{roll}} \cdot \cos\theta_{i\,\text{pitch}})^2}) \tag{17}$$

For wave energy PW_{wave} generated by the i-th oscillating buoy under regular waves with wave frequency ω, it can be also calculated in the frequency domain as:

$$PW_{\text{wave}} = \frac{1}{2}\omega^2 b_{\text{PTO}} \Delta\theta_{i\,\text{pitch}}{}^{2} \tag{18}$$

Wave energy is harvested through the relative motion between floating bodies, which depends on optimizing PTO damping. However, maximizing wave energy capture often conflicts with reducing system motion, as less motion tends to enhance photovoltaic performance due to their negative correlation. This results in a trade-off between maximizing wave energy harvesting and minimizing motion response. Since photovoltaic energy typically constitutes the majority of the total energy output, and the level of motion response directly influences the photovoltaic energy harvested, unifying the optimization objective to maximize total energy output (PW_{solar}+PW_{wave}) offers an effective strategy to balance both energy harvesting and motion control.

Table 3 Parameters of solar irradiance components

Parameter	**Value**
Solar Constant I_{sc} (W/m^2)	1367
Atmospheric Transmittance Coefficient P_{t}	0.7
Reflection Coefficient on the sea surface ρ_{w}	0.35
Declination angle on the Winter Solstice δ(°)	-23.44
Eccentricity correction factor on the Winter Solstice ξ_0	0.992
Initial tilt angle of the photovoltaic panels β_0(°)	15
Initial azimuth angle of the photovoltaic panel γ_{n}(°)	0

Table 4 List of main nomenclatures

Symbol	**Descriptions**
B_{h}	Direct beam solar irradiance (W/m^2)
D_{h}	Diffuse solar irradiance (W/m^2)

G_h	Reflected solar irradiance (W/m^2)
φ	Latitude (°)
δ	Declination angle (°)
ω	Hour angle (rad): Angular displacement of the sun from solar noon
γ_n	Azimuth angle of the panel relative to the horizontal plane (rad)
$P_{solar}(t)$, $P_{wave}(t)$	Instantaneous power output of the PV module / Instantaneous power output from the PTO system of the wave energy converter (W)
PW_{solar}, PW_{wave}	Preliminary power estimates for solar and wave systems based on motion response amplitudes in the frequency domain, used for rapid optimization (W)

4. Validation

A validation of the developed multibody hydrodynamic coupled motion simulations code is performed through a comparison with both model test results and numerical data from Zhang et al. [49]. Although the validation experiment focuses on a single-row module, the simulation methodology remains consistent for multi-floater systems under wave action, supporting its applicability to the dual-module floating photovoltaic arrays proposed in this study. The schematic of the validation model and some key properties of the floating box are given in Figure 5 and Table 5, respectively.

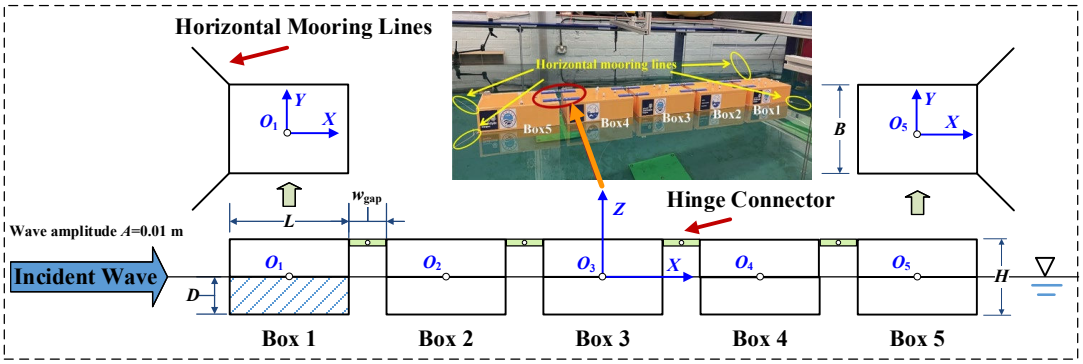

Figure 5 Schematic of the validation model of a 5-box system with hinge assembly

Table 5 Key properties of the single floating box

Module Characteristic	Value
Length, L (m)	0.4
Width, B (m)	0.25
Height, H (m)	0.2
Draught, D (m)	0.1
Mass, m (kg)	102.5
Gap Width, w_{gap} (m)	0.08
Center of gravity above base, KG (m)	-0.027
Pitch moment of inertia, M_{55} (kg·m^2)	0.128
Water Depth (m)	1.35

The model test, used for reference, was carried out at a flume tank of the Kelvin Hydrodynamic Laboratory of University of Strathclyde. The incident wave propagates along the x-axis, with a wave amplitude of 0.01 m, and the non-dimensional wave frequency ranges from 0.2566 to 1.7723. The nondimensional wave frequency $\omega_0(L/g)^{0.5}$ normalizes wave frequency using the characteristic length L and gravitational acceleration g, aiding scale-independent hydrodynamic analysis. A horizontal mooring system is used in the model test to restore the system to its original position. The pitch RAO of each floating box, obtained by the proposed numerical model, are compared in Figure 6 with both the experimental results from Ref. [49]. The results indicate good agreement between the motion response floating bodies in the proposed method and the model test, with higher peak values in the numerical results due to the neglect of viscous effects. To improve accuracy, an artificial viscous damping term was introduced in the dynamic equations, which enhances agreement with the experimental results. The selection of this viscous damping value is primarily based on empirical tuning to match the decay characteristics observed in free decay tests [50]. Notably, due to the coupling between hydrodynamics and hinge constraints, the pitch motion of the box-type floating bodies, excluding the central one, exhibits three distinct peaks within the selected wave frequency range. Also, compared to the other modules, the first and last floating bodies exhibit larger pitch responses over a wider range of wave periods. For the scale of the proposed modules, these amplified responses occur within the wave period range of approximately 4.89 to 6.35 s, which aligns well with the wave conditions investigated in this study. This provides valuable insights into the influence of floater position on motion responses and supports the proposed dual-module design.

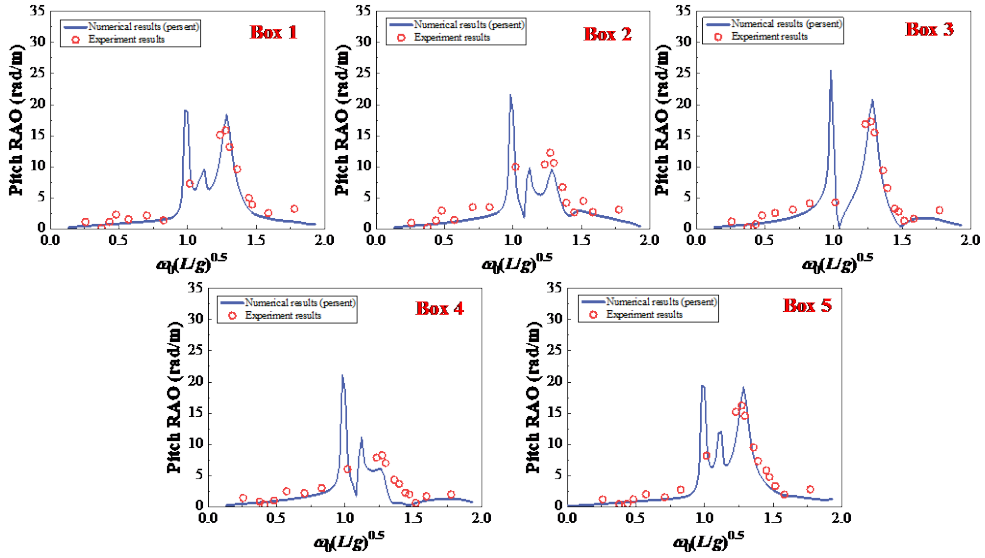

Figure 6 Comparison of the pitch RAO of the boxes between the proposed numerical model and experimental results

5. Results and discussion

5.1 Preliminary assessment the performance of the novel dual-module FPV array system

Although the dual-module FPV array design concept is derived from the motion characteristics of individual floating modules, further investigation is required to evaluate the hydrodynamic coupling between multiple floating bodies and the influence of the connector mechanism on the motion responses, to confirm the performance benefits of the integrated system. In this section, three different array configurations, as presented in Table 3, are systematically compared to assess the performance benefits of the dual-module FPV array with PTO damping: (Case A) seven semi-submersible platforms connected by hinges, (Case B) five semi-submersible platforms and two box-type modules, (Case C) five semi-submersible platforms and two box-type modules with an appropriate linear PTO damping system. The preliminary study assumes regular waves propagating in the positive x-direction, with wave periods T ranging from 0.2 s to 10 s, covering a broad spectrum of wave conditions typical for the South China Sea. To emphasize motion responses, the floating bodies are treated as unconstrained by mooring lines, focusing the analysis on their dynamic behavior.

Table 6 Three types of FPV array configurations for comparison

Case	Schematic Layout	Notes
Case A	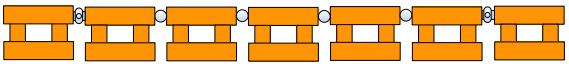	7 semi-sub modules
Case B	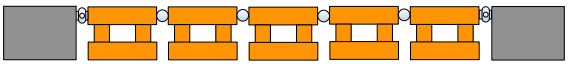	5 semi-sub modules and 2 box-type modules
Case C	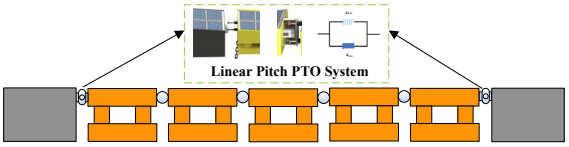	5 semi-sub modules and 2 box-type modules, with linear PTO damping b_{PTO}=1.5E+06 N*m*s/rad

The motion response RAOs of individual floating modules, including pitch and heave, as well as the hinge connection forces for the three FPV configurations, are shown in Figure 7, Figure 8 and Figure 9, respectively. The heave and pitch responses for all configurations follow similar trends, mainly due to the hinge connection design. In Case A, with seven semi-submersible platforms connected by hinges, the heave and pitch responses increase from the leading to the trailing modules. The open geometry of the platforms facilitates partial wave transmission beneath and between the structures, allowing wave energy to propagate continuously downstream with minimal attenuation. Under long-period wave conditions, this effect becomes particularly pronounced, as the transmitted, diffracted, and radiated wave

components constructively interfere, resulting in significant amplification of motion responses at the trailing modules. This amplification of motion responses leads to a corresponding increase in connection forces, which follow a similar trend. The absence of energy dissipation mechanisms in this fully passive configuration allows wave energy to propagate and accumulate across the array, further amplifying both the motion responses and the structural stress. Without damping mechanisms, wave energy accumulates across the array, stressing the need for design adjustments like reconfiguring the layout or adding damping.

Case B replaces the leading and trailing modules with box-type modules, improving energy transmission, motion control, and reducing dynamic loads. By leveraging the dual-module concept, this configuration optimizes energy transmission and structural response, enhancing motion control and reducing dynamic loads. As shown in Figure 7 (d) and Figure 8 (d), this leads to a marked reduction in the average heave and pitch responses of the FPV array, especially under long-period wave conditions. However, at shorter wave periods, a slight increase in motion is observed, likely due to the increased rigidity of the box-type modules. Nevertheless, this increase does not significantly impact the overall system performance. Similarly, Figure 9 (d) illustrates a reduction in hinge connection forces under long-period wave conditions, indicating a more balanced load distribution. This integration emphasizes the importance of the dual-module layout in optimizing motion control and system stability.

As for the approach of incorporating damping mechanisms, Case C introduces PTO damping to reduce wave-induced motions and connection forces. Expanding upon the structural improvements introduced in the dual-module layout of Case B, this configuration further optimizes motion responses by significantly reducing the pitch amplitudes of the floating modules and alleviating the dynamic loads on the hinge connections, as shown in Figure 7 (e) and Figure 9 (e). In contrast, as observed in Figure 8 (e), the heave responses remain relatively unaffected, being primarily governed by buoyancy forces, with only minor coupling effects from rotational motions. This highlights the directional specificity of pitch PTO damping, which is more effective in reducing rotational motions than vertical displacements. Additionally, the incorporation of PTO damping not only improves system stability but also enables the conversion of wave energy into usable power, contributing to the overall energy efficiency of the system. Case C thus proves highly effective, serving as the foundational configuration for subsequent analysis and optimization.

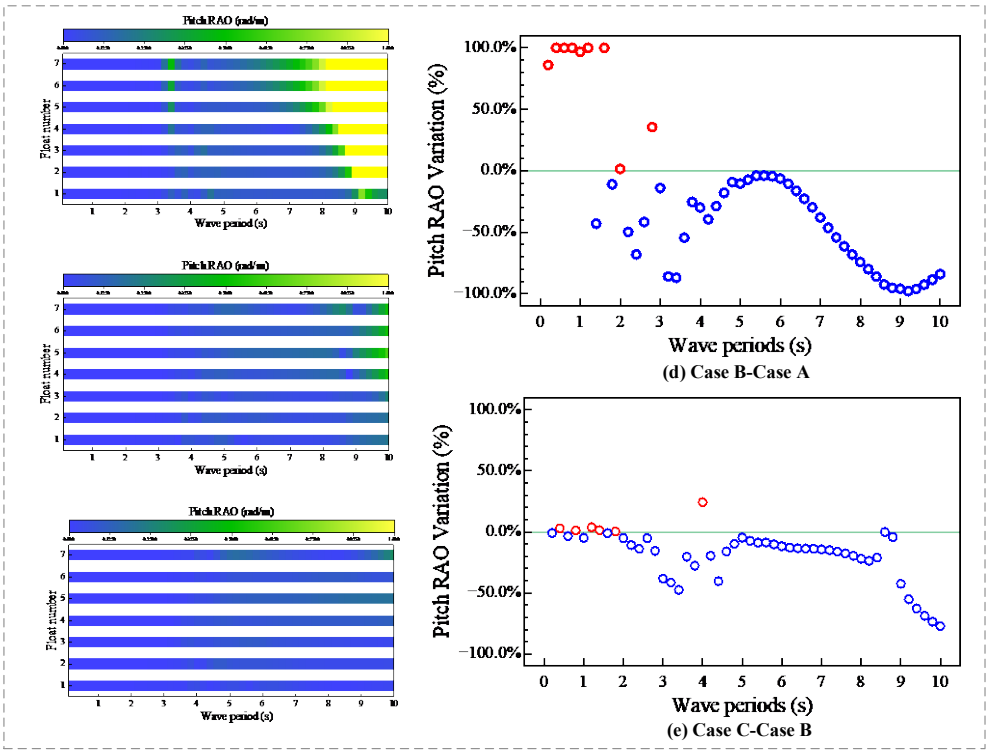

Figure 7 Comparison of pitch RAOs for three FPV array configurations

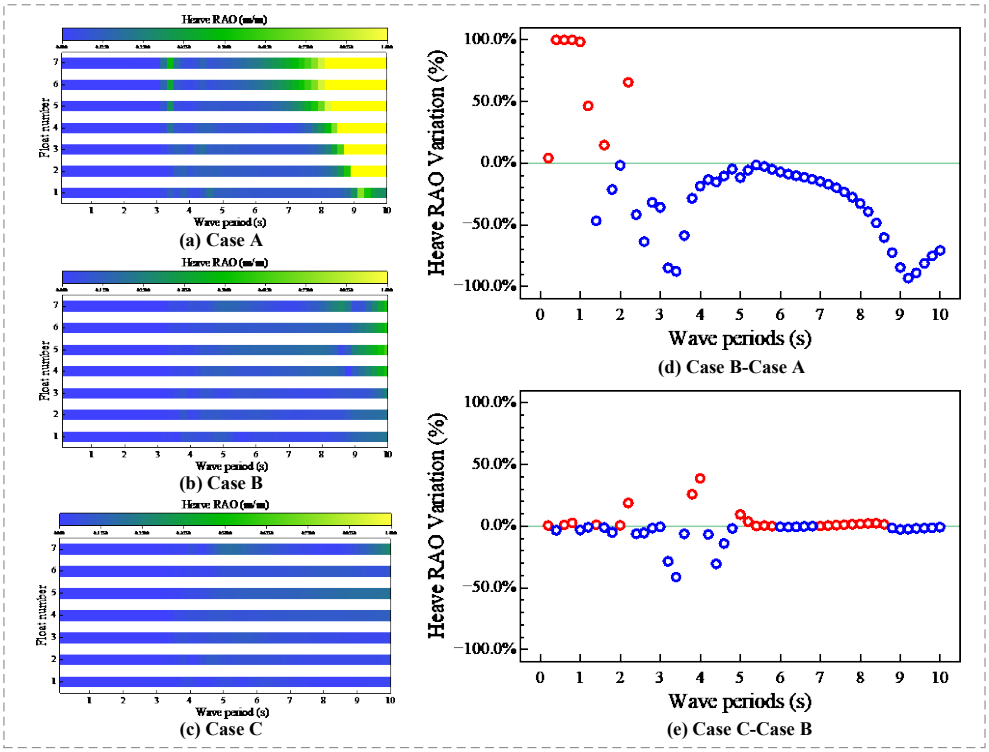

Figure 8 Comparison of heave RAOs for three FPV array configurations

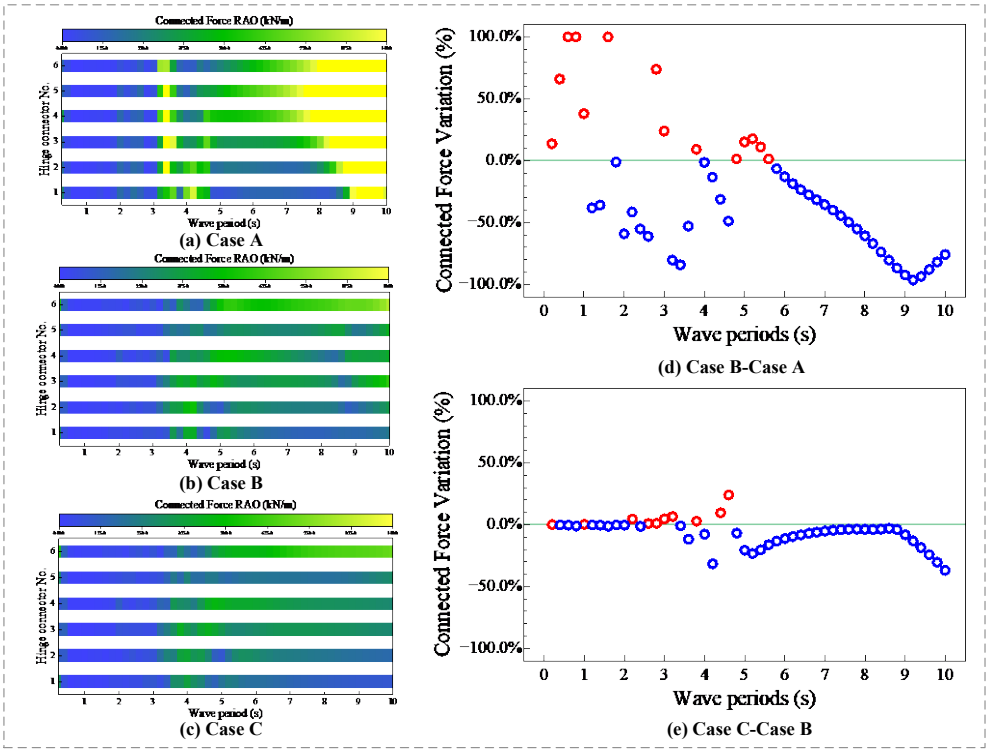

Figure 9 Comparison of connector force RAOs for three FPV array configurations

5.2 Longitudinal expansibility of a row of dual-module FPV array

FPV arrays can benefit from an increased number of modules, providing additional deck space for solar panels. However, the effect of this expansion on motion dynamics remains uncertain. This section focuses on a single-row dual-module FPV array to investigate the impact of longitudinal expansion on motion behavior, as shown in Figure 10. The array comprises box-type modules at both ends and semi-submersible modules in the middle, with the number of floating bodies varying from 5 to 9.

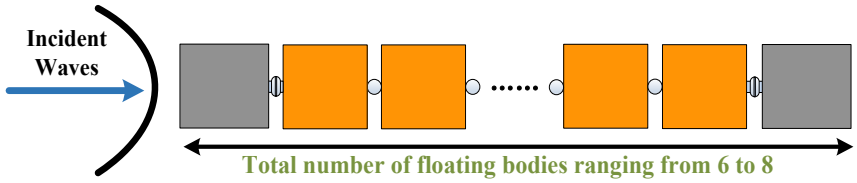

Figure 10 Top view sketch of a row of FPV array

The motion responses of a single-row array with varying numbers of floats, at incident angles of 0°, 30°, and 60°, are presented, as shown in Figure 11, Figure 12, Figure 13, respectively, for interactions with four representative wave periods (T_1=4.00 s, T_2=5.30 s, T_3=6.45 s, T_4=7.20 s). T_1 represents a short-wave period while corresponding to a motion peak in the heave RAO of the individual module. T_2 and T_3 are two intermediate waves, representing the average wave periods for the selected operating sea states. T_4 is a relatively long wave, with a wavelength similar to the total length of the array.

Comparing Figure 11 with Figure 12 and Figure 13, it is evident that motion responses under

oblique wave incidence (30° and 60°) are significantly larger than those under head-on wave incidence (0°), particularly for shorter wave periods. This is due to the more complex diffraction and radiation patterns created by oblique waves, which lead to asymmetric wave loads on the floats and amplify hydrodynamic interference among them. As wave period increases, responses for both oblique and head-on waves converge due to reduced phase differences and spatial variation across the array. At 60° incidence, the misalignment between wave direction and floater orientation enhances asymmetry, particularly under short-period waves, leading to larger pitch and heave responses than at 30° incidence. While the influence of oblique waves diminishes with longer wave periods, long-period waves generally induce larger motions due to their extended wavelengths, especially as the wave frequency approaches the natural frequencies of the array.

The number of floaters also significantly influences the hydrodynamic performance, especially for pitch and heave motions. Longer arrays generally exhibit larger pitch responses at the trailing end, especially under long-period waves, where diffraction and radiation effects are more pronounced. This is further amplified by the hinged connections between floaters, which allow for greater rotational freedom at the trailing end. Heave motion increases similarly, but its rise with additional floaters is less pronounced, stabilizing toward lower values at the trailing end of the array.

Despite variations in the number of floaters, arrays of different lengths demonstrate consistent performance trends across the four wave periods, particularly for intermediate waves. This suggests that shorter arrays can effectively approximate longer ones for preliminary design. However, shorter arrays must include a sufficient number of floaters to accurately capture key hydrodynamic interactions. Arrays that are too short may fail to represent localized responses, particularly at the trailing end, as shown in Figure 11 (a). Based on these findings, a single-row, 7-floater configuration is selected for subsequent studies, providing a balance between computational efficiency and the ability to capture essential hydrodynamic phenomena.

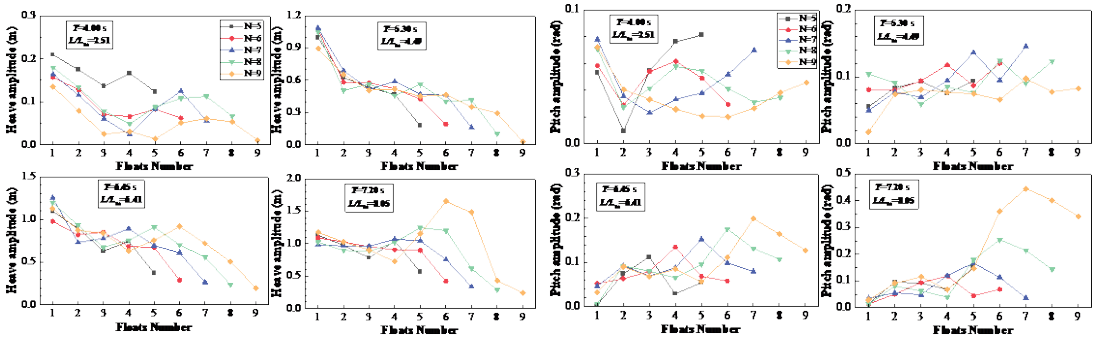

(a) Heave motion (b) Pitch motion

Figure 11 Motion responses of a single-row array with varying numbers of floats at four representative wave periods (0° wave incidence)

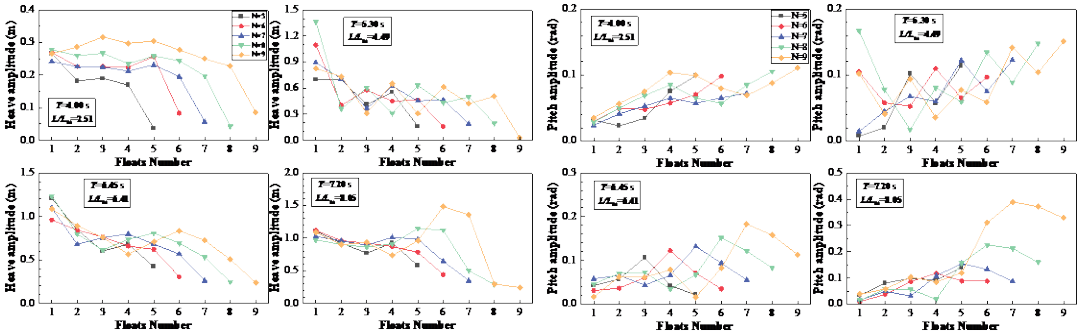

(a) Heave motion (b) Pitch motion

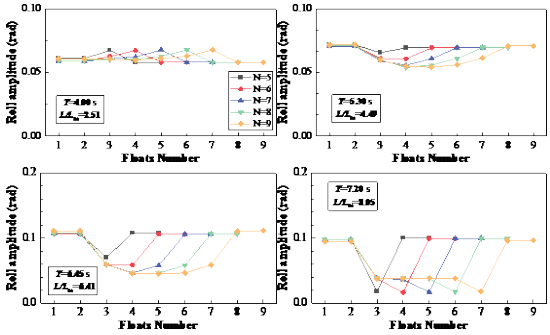

(c) Roll motion

Figure 12 Motion responses of a single-row array with varying numbers of floats at four representative wave periods (30° wave incidence)

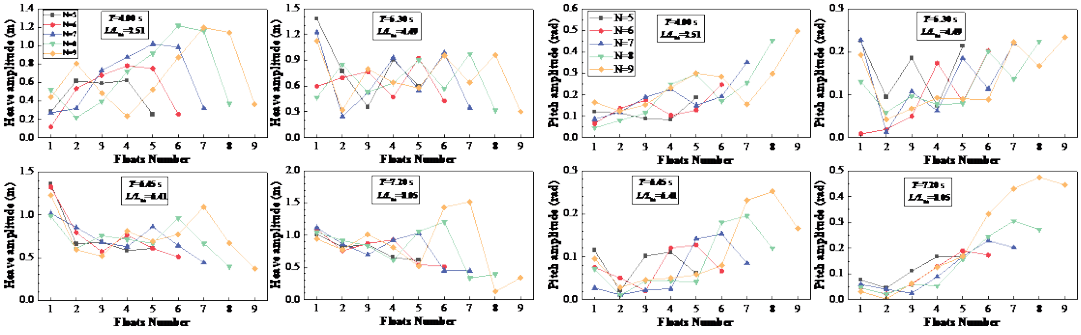

(a) Heave motion (b) Pitch motion

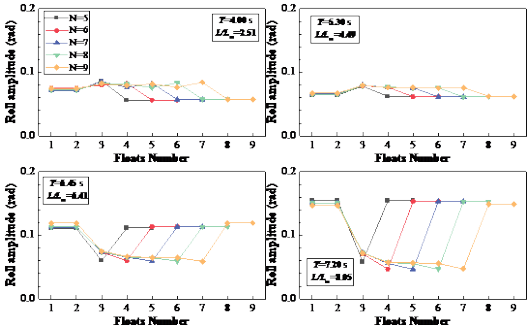

(c) Roll motion

Figure 13 Motion responses of a single-row array with varying numbers of floats at four representative wave periods (60° wave incidence)

5.3 Lateral expansibility of the dual-module FPV array configuration

The lateral expansibility of the dual-module FPV array is analyzed by examining the effect of increasing the number of rows, from 1 to 4, on the system's hydrodynamic performance. As illustrated in Figure 14, the array consists of multiple rows arranged laterally, each composed of dual-module unit. The semi-submersible floaters within each unit are connected by ball joints, allowing for relative rotational motion. The rows are uniformly spaced, with catenary mooring systems installed at both ends of the semi-submersible floaters in each uni. The equivalent stiffness matrix of the mooring system of each dual-module unit is provided in Table 7. Regular waves of T_2=5.3 s and T_3=6.45 s, representing the average wave periods at two selected operation sites, are used in the simulations. Wave incidences of 0° and 60° are considered to simulate head-on and oblique wave conditions, respectively.

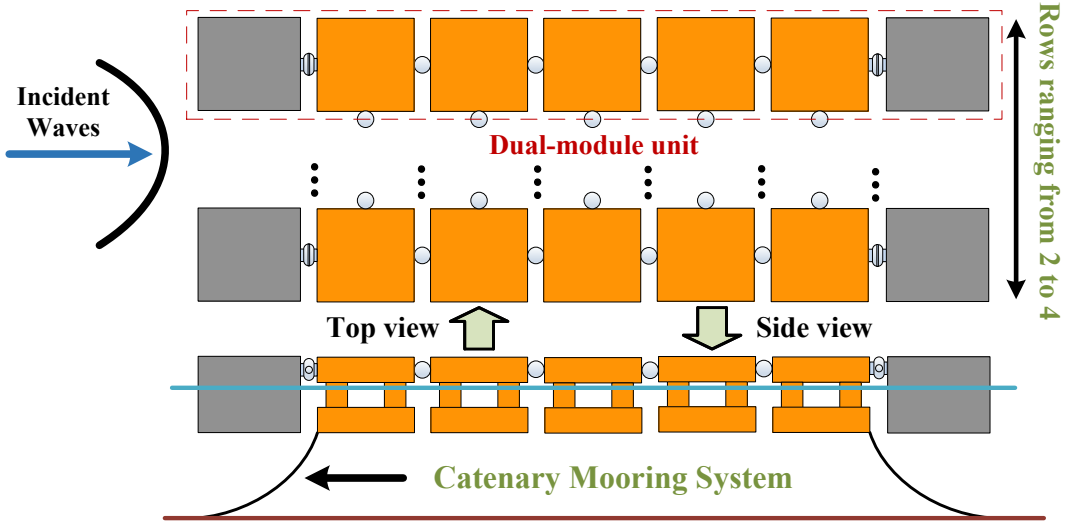

Figure 14 Top and side view sketch of FPV array configuration

Table 7 Equivalent mooring stiffness matrix of each dual-module unit [51]

(Units: Translational stiffness: $[F/x]$=N/m, Rotational stiffness: $[M/\theta]$= N·m/rad, Coupling terms: $[F/\theta]$ = N/rad and $[M/x]$ = N·m/m)

Unit Displacement/ Rotation	Force in *x* (Surge)	Force in *y* (Sway)	Force in *z* (Heave)	Moment in R*x* (Roll)	Moment in R*y* (Pitch)	Moment in R*z* (Yaw)
Displacement *x* (Surge)	1.59E+04	0	0	0	3.02E+05	0
Displacement *y* (Sway)	0	1.51E+03	0	6.06E+03	0	5.00E+04
Displacement *z* (Heave)	0	0	9.24E+03	0	-3.05E+05	0

Rotation R*x* (Roll)	0	6.06E+03	0	5.77E+05	0	2.00E+05
Rotation R*y* (Pitch)	3.02E+05	0	-3.05E+05	0	2.27E+07	0
Rotation R*z* (Yaw)	0	5.00 E+04	0	2.86 E+06	2.86E+03	5.85E+06

Figure 15 and Figure 16 present the motion responses of the floaters in the first row of the array under the specified wave conditions, investigating the hydrodynamic effects of lateral expansion. Comparing the results, the overall motion at T=5.3 s is slightly greater than that at T=6.45 s, which can be attributed to the fact that the wave period is closer to the period corresponding to the pitch motion response amplitude of the box-type floating module. The motion responses demonstrate a clear trend of convergence as the number of rows increases, reflecting the ability of the expanded configuration to distribute wave energy more evenly.

As shown in Figure 15 (a) and Figure 16 (a), under head-on wave incidence (0°), floaters closer to the wave-facing side generally experience larger motion responses due to direct wave exposure, while the trailing floaters benefit from wave attenuation caused by diffraction, radiation, and partial reflection from the preceding floaters. This effect is particularly evident in heave and pitch responses, resulting in a more uniform distribution of motion across the row. Notably, roll motion, absent in the single-row configuration, emerges in multi-row arrays due to inter-row hydrodynamic interactions. In contrast, Figure 15 (b) and Figure 16 (b) demonstrates that under oblique wave incidence (60°), the motion responses exhibit a different pattern. Due to the asymmetric wave loads introduced by the oblique wave direction, trailing floaters may experience larger motion responses, particularly in pitch and roll. The overall motion amplitudes under oblique waves are generally larger than under head-on waves at the same periods, as a result of increased diffraction and radiation complexity, along with greater hydrodynamic interference among the floaters. The box-type module configuration, designed for head-on waves, effectively reduces motion but is less effective under oblique wave conditions, particularly for trailing floaters.

A comparison of different row configurations reveals the influence of row count on the motion responses of the array. As the number of rows increases, motion responses generally decrease and stabilize, particularly for heave and pitch motions. This is attributed to the attenuation of wave energy through diffraction, radiation, and partial reflection, which reduces the amplitude of responses in multi-row arrays compared to single-row setups. However, under oblique wave incidence, roll motion increases with the number of rows up to three, after which it converges. This is due to the reduced ability of the FPV array to mitigate asymmetric wave loads under oblique wave incidence, with this effect becoming less pronounced as the number of rows increases.

To enable further expansion of the FPV array, simulating long arrays with numerous rows is challenging due to computational constraints. A limited configuration that effectively captures key hydrodynamic interactions is therefore necessary. As shown in Figure 15 and Figure 16, the three-row configuration adequately represents the primary wave-structure interactions, with motion responses for heave, pitch, and roll showing minimal variation when additional rows are added. The 3×7 configuration, comprising three rows of seven floaters each, is selected as the model for further analysis, as it effectively captures the key hydrodynamic behaviors of the FPV array under intermediate wave conditions.

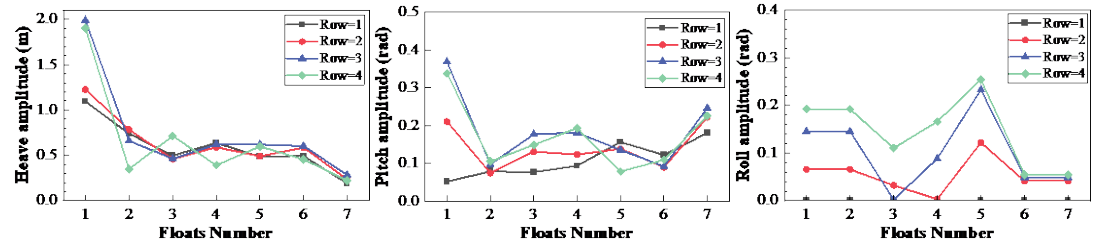

(a) 0°

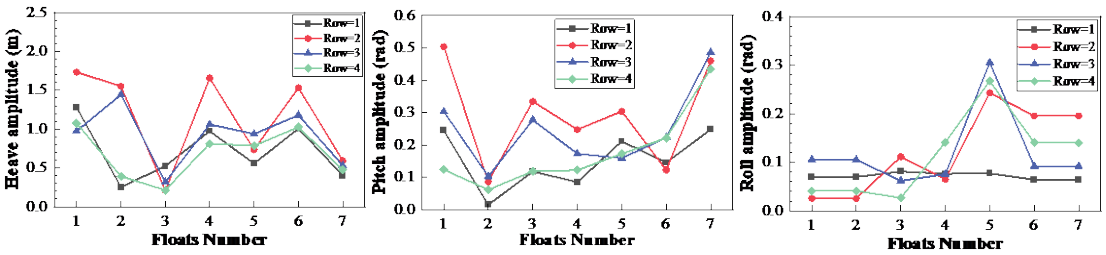

(b) 60°

Figure 15 Motion response FPV array with varying numbers of rows (T=5.30 s)

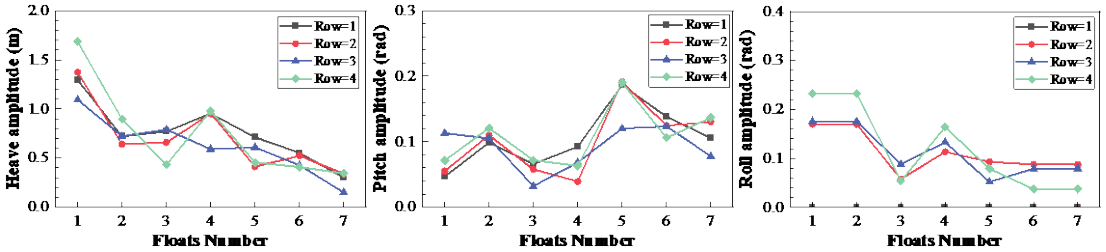

(a) 0°

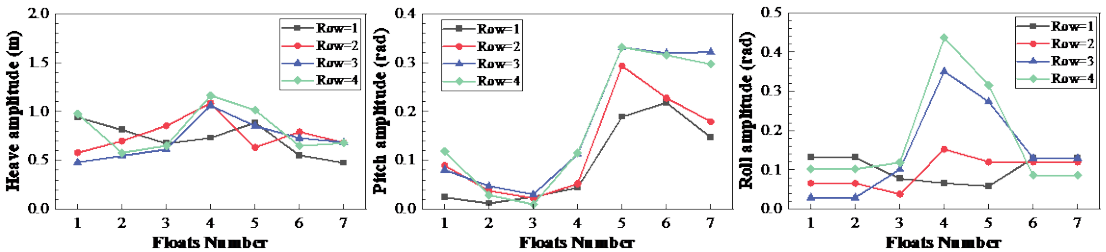

(b) 60°

Figure 16 Motion response FPV array with varying numbers of rows (T=6.45 s)

5.4 Optimization of PTO damping for enhancing system performance

The 3×7 FPV array unit selected for study has shown promising motion performance, but motion responses remain relatively large under certain conditions. To further optimize the array's hydrodynamic performance, the integration of damping mechanisms will be explored, offering potential for improvement. The proposed PTO optimization strategy iteratively adjusts the damping coefficient to maximize the total energy output, including both photovoltaic energy (PW_{solar}) and wave energy (PW_{wave}). The process evaluates the power output across a defined damping range and refines the selection based on the system's frequency-domain response [47]. By selecting the damping value that maximizes the total energy output, the strategy effectively optimizes both energy harvesting and system stability. This dual-purpose approach offers a more effective solution than entirely relying on large damping to suppress motion. The PTO damping coefficients are optimized within the range 2.00E+06 N*m*s/rad to 3.00E+07 N*m*s/rad to accommodate a wide range of wave conditions. The optimal PTO damping coefficients under various wave conditions are shown in Figure 17. Results indicate a clear correlation between the trend of the optimal damping coefficients and the pitch motion of the box-type module in the first row. Under shorter wave periods, where the motion responses of the floaters are relatively minimal, wave energy is insufficient for compensation, leading to the upper limit of the optimal damping coefficient, which minimizes motion response and enhances photovoltaic efficiency. As the wave period increases, the contribution of captured wave energy to the total generated energy rises significantly. Notably, near the resonant period of the box-type module (T=5.3 s), wave energy contributes more than 30% of the total energy output. Optimizing damping to capture more wave energy results in greater energy conversion benefits, causing the trend of the optimal damping coefficient to better align with the pitch motion of the floats. For the 60° incident waves case, the optimal damping coefficients are significantly higher than those for 0° incidence across most wave periods. This can be attributed to the larger motion responses induced by oblique wave angles, requiring higher damping for effective motion control and energy conversion.

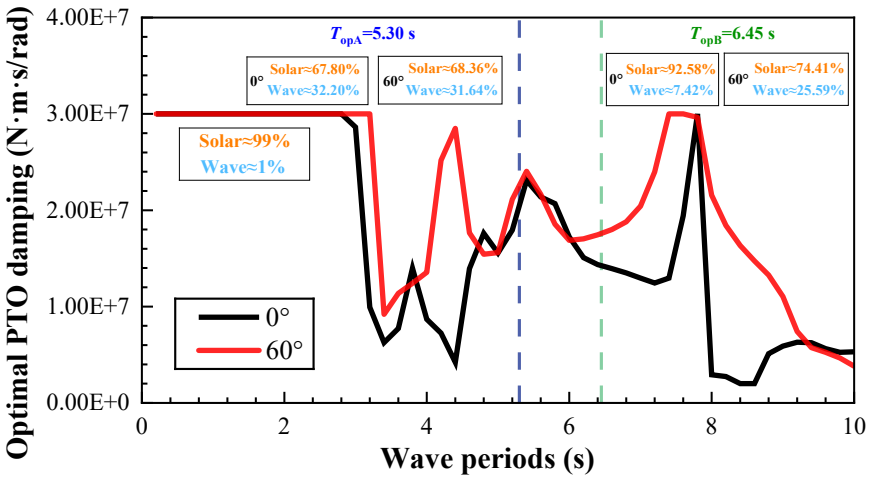

Figure 17 Optimal PTO damping under different wave conditions

While the optimal PTO damping coefficients are determined to maximize the total energy output of the system, it is also essential to assess their impact on the motion responses. The motion responses of the FPV array under two representative regular wave periods, T_{opA}=5.30 s and T_{opB}=6.45 s, corresponding to the average wave periods $\overline{T}$ at Locations A and B, as shown in Figure 18 and Figure 19, respectively.

For T_{opA}=5.30 s, the damping mechanism significantly reduces both pitch and heave motions across the array, as illustrated in Figure 18. The leading floaters of the array exhibit the largest motion responses due to direct wave exposure and the excitation of pitch motion near the resonance frequency of the box-type module, resulting in amplified dynamic responses. By incorporating optimal damping, the excess motion energy is effectively dissipated, which significantly enhance stability. In contrast, the trailing floaters, located further downstream, benefit from wave attenuation and energy redistribution due to the hydrodynamic interactions with the preceding floaters. As a result, the motion responses in the trailing floaters are generally reduced, although less significantly than the leading floaters. This is due to more complex wave-structure interactions and less wave energy reaching the last row. While the damping mechanism within the connectors still contributes to mitigating motion, its effect is less significant in the trailing positions, where the reduction in motion is more moderate. Under head-on wave incidence, the wave forces are more uniformly distributed across the array, leading to a more stable response. This symmetry reduces the potential for resonance effects, which typically amplify motion, and ensures more efficient energy dissipation by the damping system. As a result, the overall motion response of the FPV array remains relatively low, and the addition of damping further minimizes the motion, enhancing system stability. However, under oblique wave incidence, asymmetric wave loads lead to more complex hydrodynamic interactions, especially in the trailing floaters. While the damping mechanism reduces motion, including a 62.86% reduction in pitch and a 26.67% reduction in roll, its effectiveness is limited

by both the increased complexity of wave-structure interactions and the array configuration. Consequently, the overall motion responses remain larger compared to the head-on case, potentially compromising system stability and performance. As shown in Figure 19, for T_{opB}=6.45 s, as the wave frequency deviates from the resonance frequencies associated with the pitch RAO peaks of both modules, both the pitch and heave motion responses of each floater in the system are significantly reduced compared to the T_{opA} cases. While the mechanical damping still contributes to reducing the motion responses, its effect is less pronounced under this wave period, with the maximum reduction in pitch motion dropping to 25%. Similar trends are observed for both wave periods, with the system exhibiting higher motion responses under oblique wave incidence compared to head-on wave incidence. Therefore, for a comprehensive optimization of module motions, connector loads and wave energy capture, aligning the transverse direction with the predominant wave direction is recommended.

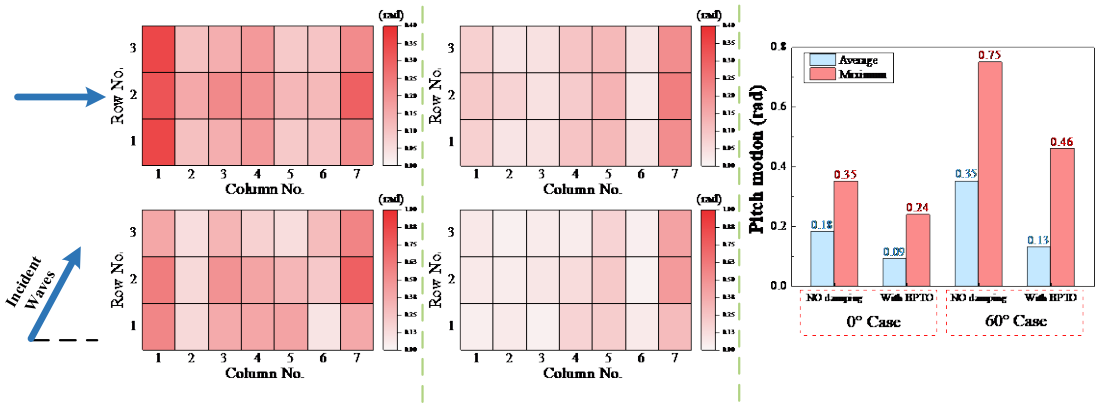

(a) Pitch motion

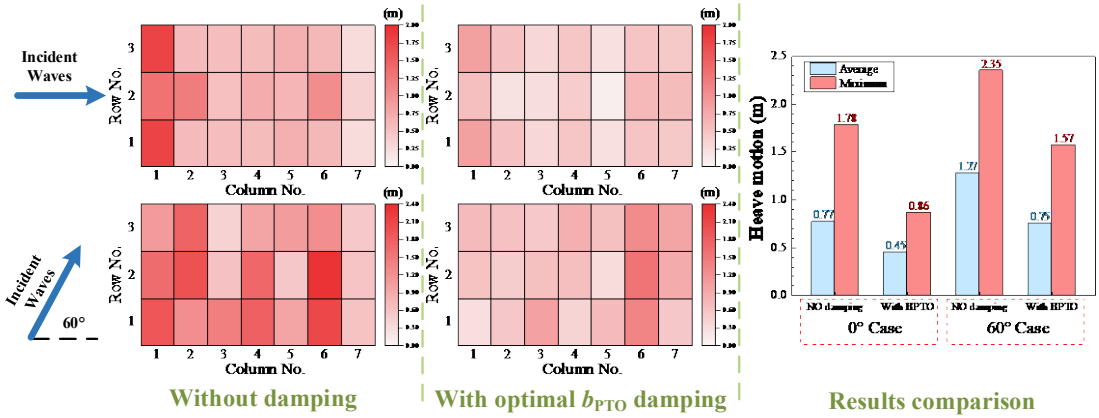

(b) Heave motion

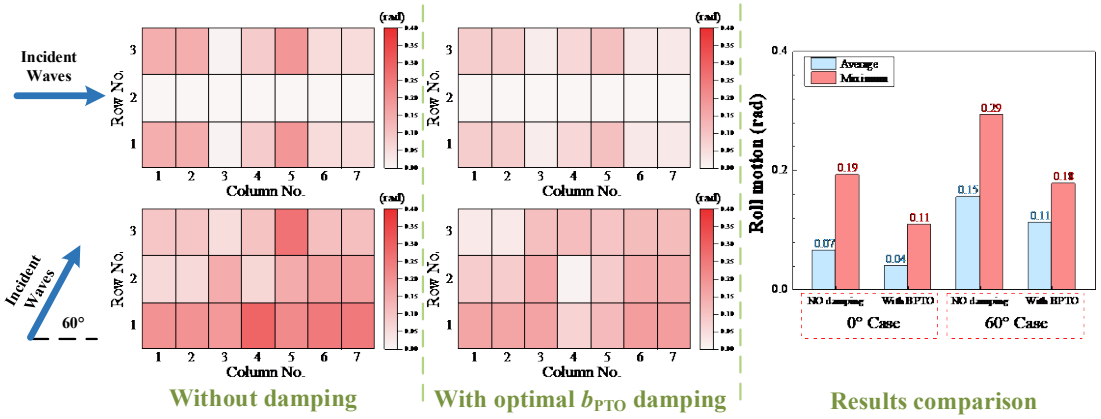

(c) Roll motion

Figure 18 Impact of optimal b_{PTO} damping on the motion response of the array at T=5.3 s

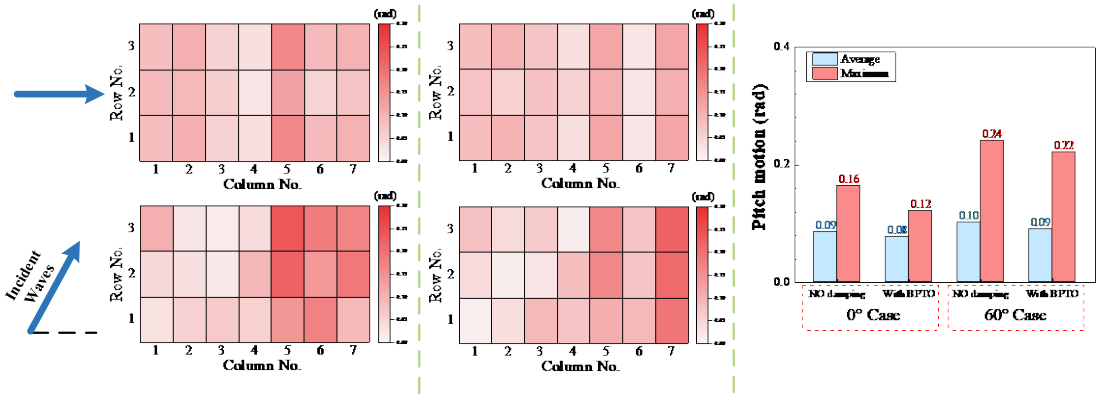

(a) Pitch motion

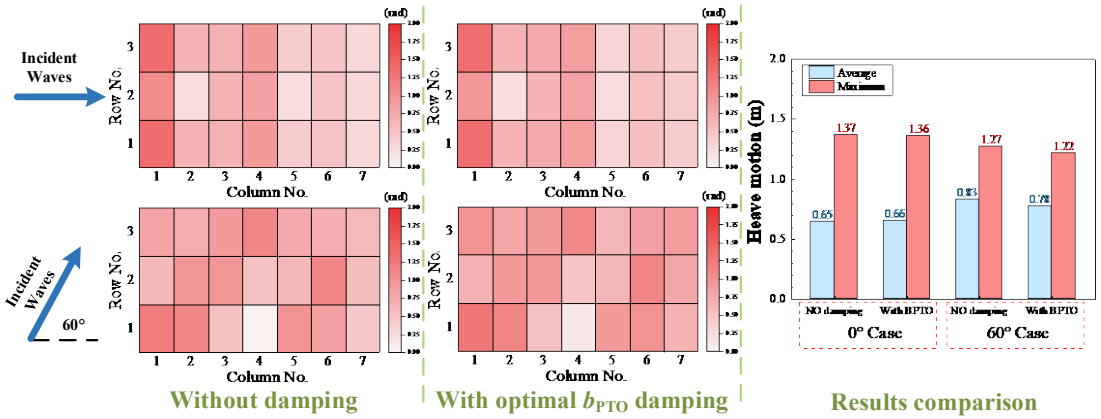

(b) Heave motion

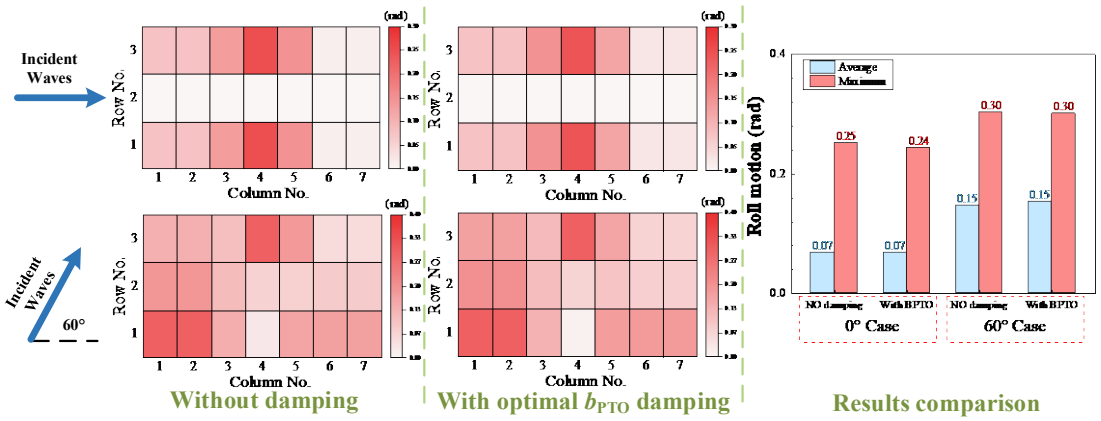

(c) Roll motion

Figure 19 Impact of optimal b_{PTO} damping on the motion response of the array at T=6.45 s

5.5 Estimation of dynamic and power performance for the selected operational site

In this section, the dynamic and power performance of the 3×7 FPV array unit is assessed under irregular wave conditions, using the JONSWAP spectrum to simulate wave environments at two representative operational sites. Figure 20 presents the motion responses of the floater with the maximum motion, which always corresponds to the leading floaters in the array. For Location B (H_s=1.63 m, $\overline{T}$ =6.45 s), which is characterized by a longer average wave period and a higher significant wave height compared to Location A (H_s=1.16 m, $\overline{T}$ =5.30 s), the increased wave energy results in more pronounced motion responses of the floaters. Nevertheless, the introduction of optimal damping continues to effectively mitigate these motions under irregular wave conditions, controlling the amplified motion induced by the varying energy components of waves with different frequencies. By reducing excessive motion, it improves both structural safety and solar energy capture by maintaining the optimal orientation of the panels relative to sunlight. The unit solar radiation of the FPV array under selected operational sites is calculated for noon on the winter solstice, assuming the photovoltaic panels are installed at a fixed tilt angle of 15° towards the south relative to the horizontal plane. A statistical comparison of the solar irradiance received by the PV panels is presented in Table 8. Despite the absence of damping, the dual-module design effectively reduces motion responses, ensuring relatively stable solar energy capture under operational sea conditions. For the two operational sites, the application of optimal PTO damping results in a slight increase in average solar radiation, while significantly reducing variability by approximately 60% in Location A, and 25% in Location B, respectively. This reduction in variability is particularly beneficial for improving the subsequent energy conversion process of the photovoltaic modules, as it helps to reduce fluctuations in solar irradiance that could otherwise cause performance mismatches between the modules.

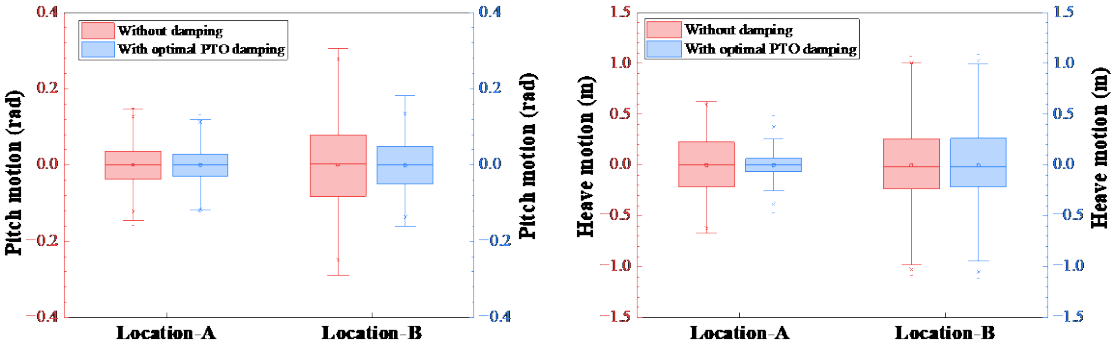

Figure 20 Box-plot of the motion responses of the float with maximum motion

Table 8 Statistical comparisons of unit solar radiation under selected operational sites

Operation Site [53]	Case	Average Solar Irradiation (W/m^2)	Standard Deviation STD (W/m^2)
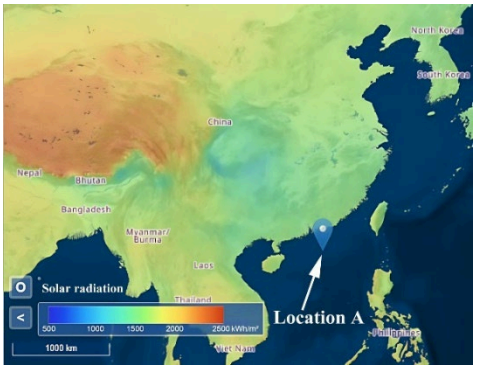 **114°58′E, 21°16′N** (H_s=1.16 m, $\overline{T}$ =5.30 s)	No damping	606.96	8.24
	With optimal b_{PTO}	612.79	3.16
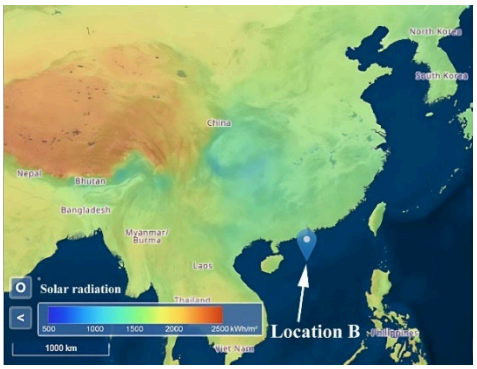 **110°39′E, 19°20′N** (H_s=1.63 m, $\overline{T}$ =6.45 s)	No damping	612.22	8.24
	With optimal b_{PTO}	619.04	5.95

Overall, it enhances both the average solar radiation and its consistency, further improving the system's solar power output across diverse wave conditions. Additionally, the PTO damping also contributes to enhanced overall system performance by facilitating the potential capture of wave energy. Additionally, the PTO damping contributes to overall system performance by enabling wave energy capture, further improving the hybrid system's overall energy generation capability. As illustrated in Figure 21, the PTO system, acting both as a motion attenuator and a wave power generator, significantly enhances the overall energy capture of the hybrid system,

with increases of 12.49% and 21.88% observed at the two operational sites, respectively. Wave power serves as an effective supplement to solar energy, further improving the hybrid system's overall energy conversion efficiency. Due to its lower latitude and higher wave energy, Location-B exhibits enhanced solar energy capture and wave energy conversion performance, benefiting from both increased solar irradiation and more intense wave conditions. However, excessive wave energy could lead to increased floater motion, reducing photovoltaic energy capture and potentially compromising system safety. Therefore, selecting an optimal operational site requires balancing these factors to ensure efficient energy capture, structural integrity, and the effectiveness of PTO damping under these wave conditions.

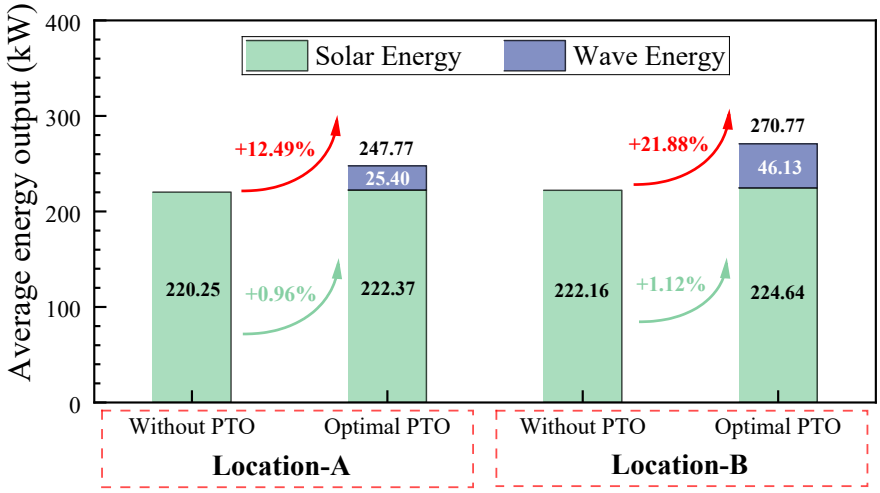

Figure 21 The power generation of the hybrid system under selected operational sites

6. Conclusions

This work presents a dual-module FPV array, combining box-type and semi-submersible modules to enhance hydrodynamic performance in the mild marine environment of the South China Sea. The influence of the array layout and PTO damping of the connectors under various wave directions and a wide range of regular wave conditions is investigated. Design optimizations are implemented to improve both hydrodynamic and energy performance. The dynamic and power generation performance of the optimized FPV array is further assessed under irregular wave conditions at two South China Sea locations, representing typical working conditions. The main conclusions are summarized as follows:

(1) The dual-module layout leverages the complementary hydrodynamic characteristics of semi-submersible and box-type modules to improve motion control and reduce dynamic loads. The centrally positioned semi-submersible modules enhance stability, while the box-type modules at the front and rear mitigate wave impact. PTO damping further improves stability and energy efficiency. By combining these two designs, the array adapts to varying environmental conditions while ensuring efficient energy production and stable operation,

offering a scalable and adaptable solution for real-world floating photovoltaic systems.

(2) In longitudinal expansion, shorter arrays with sufficient floaters approximate the response of longer arrays, balancing computational efficiency and hydrodynamic accuracy. In lateral expansion, motion responses converge after a certain number of rows, effectively capturing primary wave-structure interactions. As the array size increases, the motion response stabilizes after a certain number of modules, reducing the need for continuous design adjustments.

(3) The proposed PTO optimization strategy ensures optimal energy generation and stable operation, improving the system's practical applicability. Optimal PTO damping notably enhances system stability, particularly under head-on wave incidence, achieving a maximum reduction of 31.43% in pitch motion response.

(4) Under oblique wave incidence, damping remains effective but diminishes due to the misalignment between wave direction and array orientation, as well as more complex wave-structure interactions, resulting in relatively higher motion responses. These findings highlight the importance of aligning the array layout with the predominant wave direction to optimize module motion, connector load distribution, and wave energy capture.

(5) The incorporation of PTO damping significantly enhances the performance of the dual-module FPV array under variable wave conditions, improving both stability and solar energy capture. Motion variability is notably reduced, with optimal damping decreasing fluctuations by approximately 60% at Location A. Integrating wave energy PTO increases the hybrid system’s total energy output by more than 20% at Location B, demonstrating the potential for synergistic use of solar and wave energy. Comparative analysis shows that Location B benefits from higher wave energy and solar irradiation but experiences greater floater motion, with pitch motion increasing by 42% compared to Location A in the absence of PTO damping, potentially compromising photovoltaic performance. Thus, site selection must balance energy capture efficiency, structural stability, and PTO damping effectiveness under varying wave conditions.

Future work could focus on enhancing the energy conversion models of both the PV and PTO systems. For PV, incorporating temperature effects and inverter efficiency would improve accuracy, while practical hydraulic PTO designs with active control could further optimize energy capture.

Acknowledgements

National Natural Science Foundation of China (52222109, 52201322), Guangdong Basic and Applied Basic Research Foundation (2022B1515020036 and 2023A1515012144), Project of State Key Laboratory of Subtropical Building and Urban Science (2023ZB14).

References

[1] IEA, 2022. World energy outlook 2022. Technical Report

[2] Wei, Y., Khojasteh, D., Windt, C., & Huang, L. (2025). An interdisciplinary literature review of floating solar power plants. *Renewable and Sustainable Energy Reviews*, 209, 115094.

[3] Djalab, A., Djalab, Z., El Hammoumi, A., Tina, G. M., Motahhir, S., & Laouid, A. A. (2024). A comprehensive review of floating photovoltaic systems: Tech advances, marine environmental influences on offshore PV systems, and economic feasibility analysis. *Solar Energy*, 277, 112711.

[4] Ramanan, C. J., Lim, K. H., Kurnia, J. C., Roy, S., Bora, B. J., & Medhi, B. J. (2024). Towards sustainable power generation: Recent advancements in floating photovoltaic technologies. *Renewable and Sustainable Energy Reviews*, 194, 114322.

[5] Zhang, C., Dai, J., Ang, K. K., & Lim, H. V. (2024). Development of compliant modular floating photovoltaic farm for coastal conditions. *Renewable and Sustainable Energy Reviews*, 190, 114084.

[6] Fan, S., Ma, Z., Liu, T., Zheng, C., & Wang, H. (2025). Innovations and development trends in offshore floating photovoltaic systems: A comprehensive review. *Energy Reports*, 13, 1950-1958.

[7] Ikhennicheu, M., Danglade, B., Pascal, R., Arramounet, V., Trébaol, Q., & Gorintin, F. (2021). Analytical method for loads determination on floating solar farms in three typical environments. *Solar Energy*, 219, 34-41.

[8] Shi, W., Yan, C., Ren, Z., Yuan, Z., Liu, Y., Zheng, S., ... & Han, X. (2023). Review on the development of marine floating photovoltaic systems. *Ocean Engineering*, 286, 115560.

[9] Li, Y., Li, G., Cui, Y., Deng, W., Wang, B., Li, H., ... & Meng, H. (2024). The influence of multi-body interaction on the hydrodynamic performance of a hexagon-type floating photovoltaic. *Ocean Engineering*, 312, 119302.

[10] Xu, W., Sun, Y., & He, Z. (2024). Hydrodynamic performance study of floating photovoltaic arrays with multiple floating bodies. *Applied Ocean Research*, 153, 104286.

[11] Yan, C., Shi, W., Han, X., Li, X., & Verma, A. S. (2023). Assessing the dynamic behavior of multiconnected offshore floating photovoltaic systems under combined wave-wind loads: A comprehensive numerical analysis. *Sustainable Horizons*, 8, 100072.

[12] Zhu, K., Shi, H., Tao, J., Gong, H., Han, Z., & Cao, F. (2024). Analytical study on hydrodynamic performance of co-located offshore wind–solar farms. *Physics of Fluids*, 36(1).

[13] Li, Z., Chen, D., & Feng, X. (2023). Hydroelastic and expansibility analysis of a modular

floating photovoltaic system with multi-directional hinge connections. *Ocean Engineering*, 289, 116218.

[14] Yang, R. Y., & Yu, S. H. (2021). A study on a floating solar energy system applied in an intertidal zone. *Energies*, 14(22), 7789.

[15] Choi, S. M., Park, C. D., Cho, S. H., & Lim, B. J. (2023). Effects of various inlet angle of wind and wave loads on floating photovoltaic system considering stress distributions. *Journal of Cleaner Production*, 387, 135876.

[16] Li, M., Yang, B., Duan, J., Shu, H., Wang, Y., Yang, Z., ... & Sang, Y. (2024). Exponential slime mould algorithm based spatial arrays optimization of hybrid wind-wave-PV systems for power enhancement. *Applied Energy*, 373, 123905.

[17] Wang, B., Li, Y., Huang, L., Yao, Y., & Qin, Y. (2024). Dynamic analysis of a novel star-type floating photovoltaic system with flexible connectors. *Ocean Engineering*, 304, 117854.

[18] Claus, R., & López, M. (2023). A methodology to assess the dynamic response and the structural performance of floating photovoltaic systems. *Solar Energy*, 262, 111826.

[19] Bi, C., & Law, A. W. K. (2023). Co-locating offshore wind and floating solar farms–effect of high wind and wave conditions on solar power performance. *Energy*, 266, 126437.

[20] Jiang, Z., Dai, J., Saettone, S., Tørå, G., He, Z., Bashir, M., & Souto-Iglesias, A. (2023). Design and model test of a soft-connected lattice-structured floating solar photovoltaic concept for harsh offshore conditions. *Marine Structures*, 90, 103426.

[21] Song, J., Kim, J., Chung, W. C., Jung, D., Kang, Y. J., & Kim, S. (2023). Wave-induced structural response analysis of the supporting frames for multiconnected offshore floating photovoltaic units installed in the inner harbor. *Ocean Engineering*, 271, 113812.

[22] Sree, D. K., Law, A. W. K., Pang, D. S. C., Tan, S. T., Wang, C. L., Kew, J. H., ... & Lim, V. H. (2022). Fluid-structural analysis of modular floating solar farms under wave motion. *Solar energy*, 233, 161-181.

[23] Ji, C., Gao, X., & Xu, S. (2024). Study on the influence of connector designs on the hydrodynamic performance of an offshore floating photovoltaic. *Ocean Engineering*, 308, 118298.

[24] Wei, Y., Zou, D., Zhang, D., Zhang, C., Ou, B., Riyadi, S., ... & Huang, L. (2024). Motion characteristics of a modularized floating solar farm in waves. *Physics of Fluids*, 36(3).

[25] Zheng, S. M., Zhang, Y. H., Zhang, Y. L., & Sheng, W. A. (2015). Numerical study on the dynamics of a two-raft wave energy conversion device. *Journal of Fluids and Structures*, 58, 271-290.

[26] Han, Z., Jin, S., Greaves, D., Hann, M., & Shi, H. (2024). Study on the energy capture

spectrum of a two-body hinged-raft wave energy converter. *Energy*, 304, 132057.

[27] Wang, J., Guo, L., Wei, C., Yan, X., Huang, S., & Liu, Y. (2025). Study on the energy harvesting and hydrodynamic stability characteristics of a novel floating bridge with wave energy conversion modules. *Physics of Fluids*, 37(2).

[28] Zheng, Z., Jin, P., Huang, Q., Zhou, B., Xiang, R., Zhou, Z., & Huang, L. (2024). Motion response and energy harvesting of multi-module floating photovoltaics in seas. *Ocean Engineering*, 310, 118760.

[29] Vasuki, S. S., Levell, J., Santbergen, R., & Isabella, O. (2025). A technical review on the energy yield estimation of offshore floating photovoltaic systems. *Renewable and Sustainable Energy Reviews*, 216, 115596.

[30] Yang, Y., Mi, C., Ou, B., Wong, A., Duffy, J. G., Wood, T., ... & Huang, L. (2024). A comparative experimental study on the hydrodynamic performance of two floating solar structures with a breakwater in waves. *Solar Energy*, 284, 113029.

[31] Tay, Z. Y. (2024). Performance of integrated FB and WEC for offshore floating solar photovoltaic farm considering the effect of hydroelasticity. *Ocean Engineering*, 312, 119165.

[32] Liu, Y., Ren, N., & Ou, J. (2022). Hydrodynamic analysis of a hybrid modular floating structure system and its expansibility. *Ships and Offshore Structures*, 17(10), 2367-2377.

[33] Meng, Y., Liang, B., Gao, H., & Shao, Z. (2024). Analysis and extreme event prediction of waves in the eastern shelf seas of China based on a 44-year hindcast. *Ocean Engineering*, 312, 119102.

[34] Zhou, B. Z., Zheng, Z., Wang, Y., Jin, P., Cui, L., & Cheng, L. (2023). Optimization of an annular wave energy converter in a wind-wave hybrid system. *Journal of Hydrodynamics*, 35(2), 338-350.

[35] Liu, Y., Ren, N., & Ou, J. (2022). Hydrodynamic analysis of a hybrid modular floating structure system under different wave directions. *Applied Ocean Research*, 126, 103264.

[36] LONGi. Hi-MO 7 PV Modules. Available online: https://www.longi.com/en/products/modules/hi-mo-7/ [Accessed on 13 May 2025].

[37] Teng, B., & Taylor, R. E. (1995). New higher-order boundary element methods for wave diffraction/radiation. *Applied Ocean Research*, 17(2), 71-77.

[38] Ren, N., Zhang, C., Magee, A. R., Hellan, Ø., Dai, J., & Ang, K. K. (2019). Hydrodynamic analysis of a modular multi-purpose floating structure system with different outermost connector types. *Ocean Engineering*, 176, 158-168.

[39] Shabana, A. A. (2020). Dynamics of multibody systems. Cambridge university press.

[40] Cummins, W. (1962) The impulse response function and ship motions. Schiffstechnik, 9,

101–109.

[41] Zhou, B., Hu, J., Wang, Y., Jin, P., Jing, F., & Ning, D. (2023). Coupled dynamic and power generation characteristics of a hybrid system consisting of a semi-submersible wind turbine and an array of heaving wave energy converters. *Renewable Energy*, 214, 23-38.

[42] Padovan, A., & Del Col, D. (2010). Measurement and modeling of solar irradiance components on horizontal and tilted planes. *Solar Energy*, 84(12), 2068-2084.

[43] Bugeja, R., Mule'Stagno, L., & Branche, N. (2021). The effect of wave response motion on the insolation on offshore photovoltaic installations. *Solar Energy Advances*, 1, 100008.

[44] Tao, C., Shanxu, D., & Changsong, C. (2010, June). Forecasting power output for grid-connected photovoltaic power system without using solar radiation measurement. In The 2nd International Symposium on Power Electronics for Distributed Generation Systems (pp. 773-777). IEEE.

[45] Liu, C., Yang, Q., & Bao, G. (2017). Performance investigation of a two-raft-type wave energy converter with hydraulic power take-off unit. *Applied Ocean Research*, 62, 139-155.

[46] Jin, P., Zheng, Z., Zhou, Z., Zhou, B., Wang, L., Yang, Y., & Liu, Y. (2023). Optimization and evaluation of a semi-submersible wind turbine and oscillating body wave energy converters hybrid system. *Energy*, 282, 128889.

[47] Zhou, B., Hu, J., Jin, P., Sun, K., Li, Y., & Ning, D. (2023). Power performance and motion response of a floating wind platform and multiple heaving wave energy converters hybrid system. *Energy*, 265, 126314.

[48] Huang, L., Yang, Y., Khojasteh, D., Ou, B., & Luo, Z. (2024). Floating solar power loss due to motions induced by ocean waves: An experimental study. *Ocean Engineering*, 312, 118988.

[49] Zhang, D., Du, J., Yuan, Z., Yu, S., & Li, H. (2023). Motion characteristics of large arrays of modularized floating bodies with hinge connections. *Physics of Fluids*, *35*(7).

[50] Zhou, B., Huang, X., Lin, C., Zhang, H., Peng, J., Nie, Z., & Jin, P. (2024). Experimental study of a WEC array-floating breakwater hybrid system in multiple-degree-of-freedom motion. *Applied Energy*, 371, 123694.

[51] Zhang, H., Zhou, B., Zang, J., Vogel, C., Jin, P., & Ning, D. (2021). Optimization of a three-dimensional hybrid system combining a floating breakwater and a wave energy converter array. *Energy Conversion and Management*, 247, 114717.

[52] Maghami, M. R., Hizam, H., Gomes, C., Radzi, M. A., Rezadad, M. I., & Hajighorbani, S. (2016). Power loss due to soiling on solar panel: A review. *Renewable and Sustainable Energy Reviews*, 59, 1307-1316.

[53] Joint Research Centre - European Commission. Photovoltaic Geographical Information System (PVGIS) [Online]. 2025. Available from: https://re.jrc.ec.europa.eu/pvg_tools/en/ [Accessed 24 Mar. 2025].

Optimization of dual-module floating photovoltaic arrays: layout configuration and damping mechanisms for enhanced stability and energy performance

Zheng, Zhi

2025-09-01

Zheng Z, Hu J, Huang Q, et al., (2025) Optimization of dual-module floating photovoltaic arrays: layout configuration and damping mechanisms for enhanced stability and energy performance. Energy, Volume 330, September 2025, Article number 136879

https://doi.org/10.1016/j.energy.2025.136879